Supporting Information for

Synthetic History Matters: Understanding the Structure-Property Evolution in $CsSn_xGe_{1-x}Br_3$ Perovskites

Riley W. Hooper[1,2], Brian B. Phan[1], Trinanjan Dey[1], Cole Butler[1], Diganta Sarkar[1], Chuyi Ni[1], Arthur Mar[1], Jonathan G. C. Veinot[1], and Vladimir K. Michaelis[1,*]

[1]Department of Chemistry, University of Alberta, Edmonton, Alberta, Canada T6G 2G2

[2] Current address: Technical University of Munich, TUM School of Natural Sciences, Chemistry Department, Lichtenbergstraße 4,85748 Garching bei München, Germany

[3] Current address: Université Grenoble Alpes, CEA, IRIG, MEM, Grenoble, 38000 France

*Corresponding author: vladimir.michaelis@ualberta.ca

Table of Contents

Materials and methods S4

Solution synthesis S4

Mechanochemical synthesis S4

High temperature synthesis S5

Powder XRD S5

Single crystal XRD S6

Solid-state NMR spectroscopy S7

NMR processing and analysis S8

^{81}Br Nuclear quadrupolar resonance (NQR) spectroscopy S8

Quantum chemical computations S9

Diffuse reflectance spectroscopy S9

Raman spectroscopy S10

Scanning electron microscopy and energy dispersive X-ray spectroscopy S10

EPR spectroscopy S10

Rietveld refinements S11

$CsSn_xGe_{1-x}Br_3$ (SS) S11

$CsSn_xGe_{1-x}Br_3$ (MCS) S12

$CsSn_xGe_{1-x}Br_3$ (HT) S13

SCXRD S16

^{133}Cs T_1 data S19

$CsSn_xGe_{1-x}Br_3$ SS S19

$CsSn_xGe_{1-x}Br_3$ MCS S19

$CsSn_xGe_{1-x}Br_3$ HT S19

DRS plots S20

$CsSn_xGe_{1-x}Br_3$ SS S20

$CsSn_xGe_{1-x}Br_3$ MCS S20

$CsSn_xGe_{1-x}Br_3$ HT S20

EDX analysis S21

$CsSn_xGe_{1-x}Br_3$ SS S22

x = 0 ..... S22

x = 0.50 ..... S23

x = 1 ..... S24

$CsSn_xGe_{1-x}Br_3$ MCS S25

x = 0 ..... S25
x = 0.10 ..... S26
x = 0.25 ..... S27
x = 0.50 ..... S28
x = 0.75 ..... S29
x = 0.90 ..... S30
x = 1 ..... S31
$CsSn_xGe_{1-x}Br_3$ HT S32
x = 0 ..... S32
x = 0.50 ..... S33
x = 1 ..... S34
Additional NMR spectra S35
EPR S37
^{81}Br NQR spectra S38
Calculated NMR parameters S39
$CsSn_xGe_{1-x}Br_3$ MCS S39
$CsSn_xGe_{1-x}Br_3$ SS S40
$CsSn_xGe_{1-x}Br_3$ HT S41
References S42

Materials and methods

CsBr (99.999%), $GeBr_2$ (97%), $SnBr_2$ (55.4-59.4% Br), GeO_2 (99.99+%), and 50% aqueous H_3PO_2 were purchased from Sigma Aldrich. SnO (99.9%) was purchased from Alfa Aesar. 48% aqueous HBr was purchased from Thermo Scientific. All materials were used as received.

Solution synthesis

$CsSn_xGe_{1-x}Br_3$ (x = 0, 0.50, 1.0) samples on a ~0.5 g scale were prepared according to similar procedures for $CsSnX_3$ (X = Cl, Br, I).[1] Stoichiometric amounts of $SnBr_2$ and $GeBr_2$ were combined with excess aqueous H_3PO_2 and HBr in an argon-charged three-neck round-bottom flask. The mixture was stirred using a Teflon-coated magnetic stir bar and heated at 110 ºC for 3 h. A stoichiometric amount of CsBr was added, resulting in a precipitate (yellow $CsGeBr_3$, red-brown $CsSn_{0.5}Ge_{0.5}Br_3$, and black $CsSnBr_3$), after which heating and stirring were stopped. The products were left to cool overnight, collected by vacuum filtration, washed with a few drops of aqueous HBr, and dried under vacuum on a Schlenk line.

Mechanochemical synthesis

$CsSn_xGe_{1-x}Br_3$ (x = 0, 0.10, 0.25, 0.50, 0.75, 0.90, 1.0) samples were prepared by placing stoichiometric amounts of $SnBr_2$ and $GeBr_2$ in a 125 mL stainless steel ball mill capsule with 5 mm stainless steel balls occupying approximately a third of the capsule in a nitrogen-filled glovebox. The capsule was sealed in the glovebox and subjected to ball milling on a Retsch PM 100 Planetary Mill for 3 h at 650 rpm, with the rotation direction reversing every 10 minutes. After each hour, the capsule was opened in the glovebox and powder was redispersed within the capsule using a spatula. The milling was then resumed for the next one-hour cycle. Colour changes were evident as the products were formed (yellow-red for Ge-rich compositions vs black for Sn-rich compositions).

High temperature synthesis

$CsSn_xGe_{1-x}Br_3$ (x = 0, 0.50, 1.0) samples were prepared by high-temperature solid-state reactions. Stoichiometric amounts of CsBr, $SnBr_2$, and $GeBr_2$ were ground, cold-pressed into pellets (7 mm diameter), and loaded into carbon-coated fused silica tubes (8 mm diameter, 15 cm length) in a nitrogen-filled glovebox. The tubes were evacuated, sealed, and placed in a box furnace, where they were heated to 500 °C over 16 h, kept there for 5 d, and quenched in ice water. The $CsSnBr_3$ sample was reground and reloaded into new tubes, and subjected to a repeated heat treatment followed by a slow-cooling step of 1 °C/h to promote crystal growth. All samples were stored in a nitrogen-filled glovebox. $CsGeBr_3$ is yellow, $CsSn_{0.5}Ge_{0.5}Br_3$ is red-brown, and $CsSnBr_3$ is black.

Powder XRD

Powder XRD patterns were collected on a Bruker D8 Advance diffractometer equipped with a Cu radiation source ($K\alpha_1$ 1.5406 Å, $K\alpha_2$ 1.5444 Å) operated at 40 kV and 40 mA. Samples were placed on a zero-background Si wafer on top of a polymethylmethacrylate sample holder, dispersed with a small amount of hexane to attain constant sample height and to minimize preferred orientation. Patterns were scanned over a 2θ range of 5–90° with a step size of 0.0354° per second. Attempts were made to collect high-resolution patterns over a 9 h scan time at a step size of 0.00875° per second, but the samples degraded during data collection due to their high air and moisture sensitivity.

Rietveld refinements were carried out using TOPAS Academic.[2] Instrument parameters were included, and the background was modelled by a 12-term polynomial function. Bragg peaks and intensities were fitted to either trigonal ($R3m$) or cubic ($Pm\bar{3}m$) structural models of the perovskite phases (Figures S1–S3).[3, 4] Where appropriate, atomic positions and isotropic displacement parameters for each atom were refined, whereas site occupancies were fixed to values based on additional information from NMR and EDX analyses. Attempts were made to fit peak profiles to a combined Lorentzian-Gaussian function to account for crystallite size and strain, but the quantification was deemed

unreliable. Relative amounts of the various phases observed in the patterns were quantified. Refinement results are listed in Tables S1–S2. Refined structures from the parent compounds for each synthetic route were used as the inputs for DFT calculations (see below for computational details).

Single crystal XRD

Two single crystals with slightly different appearances were selected from the HT-prepared sample of $CsSn_{0.5}Ge_{0.5}Br_3$. Intensity data were collected at room temperature using ω scans at 8 different ϕ angles with a frame width of 0.3° and exposure times of 10 s per frame on a Bruker PLATFORM diffractometer equipped with a graphite-monochromated Mo Kα radiation source and a SMART APEX II CCD detector. Multiscan absorption corrections were applied using SADABS. Structure refinements were carried out using the SHELXTL program package.[5, 6] Crystal data, atomic positions, and interatomic distances are listed in Tables S3–S5.

Based on previous structural reports of the end members ($R3m$ for $CsGeBr_3$ and $Pm\bar{3}m$ for $CsSnBr_3$), both trigonal and cubic models were considered for $CsSn_{0.5}Ge_{0.5}Br_3$, but distinguishing between them proved to be challenging. Intensity statistics were ambiguous (R_{int} = 0.114 vs. 0.105 for crystal 1, and R_{int} = 0.125 vs. 131 for crystal 2, for trigonal vs. cubic lattices, respectively). If the conventional triply primitive cell for the $R3m$ structure is transformed to a primitive rhombohedral cell, the cell angle α is 89.4–89.5°, close to 90°. When occupancies of the tetrel site were refined, they converged to values corresponding to similar chemical formulas of $CsSn_{0.57(3)}Ge_{0.43(3)}Br_3$ or $CsSn_{0.56(4)}Ge_{0.44(4)}Br_3$ for crystal 1, and $CsSn_{0.58(2)}Ge_{0.42(2)}Br_3$ or $CsSn_{0.61(3)}Ge_{0.39(2)}Br_3$ for crystal 2, which are slightly Sn-richer compared to the loaded nominal composition of $CsSn_{0.5}Ge_{0.5}Br_3$. The cubic model tended to give slightly better agreement factors [$R(F)$ = 0.031 for cubic vs 0.043 for trigonal structure for crystal 1; $R(F)$ = 0.030 for cubic vs 0.044 for trigonal structure for crystal 2] and slightly cleaner difference electron density maps. For both trigonal and cubic models, the Br atoms always showed slightly elevated displacement parameters compared to the other atoms; this observation is consistent

with a "dynamic disorder" often proposed in the literature for related perovskites, but other more mundane explanations are possible. For the trigonal models, the tetrel atoms exhibit bond angles formed by the surrounding Br atoms of 88(1)–92(1)° for crystal 1 and 89.5(6)–90.6(6)° for crystal 2, indicating that they are nearly indistinguishable from the undistorted ideal octahedra found in the cubic models.

Five other crystals were selected for structure determination, yielding results similar to those above.

Solid-state NMR spectroscopy

^{133}Cs NMR data were acquired on a Bruker AVANCE NEO 600 NMR spectrometer (B_0 = 14.1 T) equipped with a 3.2 mm double-resonance (HX) Bruker magic-angle spinning (MAS) probe. MAS NMR spectra were acquired at natural abundance using a Bloch-decay experiment with a 5.5 μs π/2 pulse (ν_{rf} = 45.5 kHz), 4-16 co-added transients, recycle delays ≥ 1.5×T_1, and a spinning frequency of 15 kHz. The ^{133}Cs NMR spectra at 14.1 T were referenced to a secondary standard (solid CsCl; δ(^{133}Cs) = 223.2 ppm) with respect to 0.5 M CsCl (δ(^{133}Cs) = 0.00 ppm).[7] ^{133}Cs spin-lattice relaxation (T_1) measurements were carried out *via* a saturation recovery pulse sequence with a 5.5 μs π/2 pulse, 2 scans, 0.1 s recycle delay, 64 pre-saturation pulses, and variable delay times from 1 μs to 8000 s. T_1 curves were processed and fit using the Dynamics Center implemented in Topspin 4.3.0 using the SatRec function and manually determined integral regions. T_1 values were extracted from the fit curve, where the equation of fit was: $I(t) = I(0)\left(1 - e^{-\frac{t}{T_1}}\right)$.

^{119}Sn NMR spectroscopy was performed on a Bruker AVANCE NEO 500 NMR spectrometer (B_0 = 11.75 T) on a 4 mm triple resonance (HXY) Bruker MAS probe operating in double resonance mode. Experiments were performed on samples at natural abundance using a Hahn echo (HE) sequence under both spinning (MAS, ν_r = 14 kHz) and non-spinning conditions with a 4.0 μs π/2 pulse (ν_{rf} = 62.5 kHz) with 64-260k scans, and 1 s recycle delays. The ^{119}Sn NMR spectra were referenced to a secondary

standard (solid tetramethylcyclohexyltin; $\delta(^{119}Sn) = -97.35$ ppm) with respect to tetramethyltin ($\delta(^{119}Sn) = 0$ ppm).[8]

Non-spinning ^{73}Ge NMR spectra for SS and MCS $CsGeBr_3$ were acquired at natural abundance on a Bruker AVANCE NEO 800 NMR spectrometer ($B_0 = 18.8$ T) using a 4 mm low-γ double resonance (HX) Bruker MAS probe. Spectra were collected using a quad-echo ($\pi/2_x$ -τ- $\pi/2_y$) with a 4.0 μs π/2 pulse ($\nu_{rf} = 62.5$ kHz), 200-300 μs interpulse delay, 3-6 M co-added transients and a recycle delay of 0.1 seconds. ^{73}Ge NMR spectra were referenced to a tertiary standard (microcrystalline Ge powder; $\delta(^{73}Ge) = -73.8$ ppm) with respect to liquid $GeCl_4$ ($\delta(^{73}Ge) = 30.9$ ppm).[9]

A non-spinning ^{73}Ge NMR spectrum for HT $CsGeBr_3$ was acquired at natural abundance on a Bruker AVANCE II 900 NMR spectrometer ($B_0 = 21.1$ T) using a 7 mm single resonance MAS Bruker probe. Spectra were collected using a quad-echo ($\pi/2_x$ -τ- $\pi/2_y$) with a 4.0 μs π/2 pulse ($\nu_{rf} = 62.5$ kHz), 500 μs interpulse delay, 160k co-added transients and a recycle delay of 0.4 seconds. ^{73}Ge NMR spectra were referenced to a secondary standard (liquid $GeCl_4$ to 30.9 ppm) with respect to GeH_4 ($\delta(^{73}Ge) = 0.00$ ppm).[10]

NMR processing and analysis

All NMR spectra were processed with Bruker TopSpin 4.3.0. NMR spectra were fit using the QUEST NMR simulation program.[11] Errors in NMR parameters were determined in QUEST by manually altering NMR parameters to within reasonable tolerances (the error is then the distance in either direction from the centre of the acceptable parameter range). Data were plotted and analyzed in Origin 2024.

^{81}Br Nuclear quadrupolar resonance (NQR) spectroscopy

NQR measurements were performed using a 5 mm Chemagnetics probe connected to a Bruker Avance NEO console, isolated approximately 6 m away from the nearest unshielded magnet (^1H ν_L = 300 MHz; 7.05 T). Hahn echo experiments were acquired for samples at natural abundance with a 4 μs

$\pi/2$ pulse (ν_{rf} = 62.5 kHz), with 16k (MCS and HT) or 6400 (SS) co-added transients, recycle delays of 0.05 s, and summed in a VOCS approach,[12] where necessary, by stepping the transmitter frequency in steps of 50 kHz. Tuning ranges were adjusted over ~40 MHz by manually changing capacitors. The measured field at the probe head is approximately 100 μT, determined using a built-in smartphone magnetometer.

Quantum chemical computations

Density functional theory (DFT) computations were performed using the CASTEP[13] and NMR CASTEP[14-16] software packages, which use the gauge-including projector augmented waves (GIPAW) method for computing NMR properties of periodic structures.[14, 17] NMR calculations were performed using the Perdew-Burke-Ernzerhof (PBE)[18] generalized gradient approximation (GGA) exchange-correlation functional, ultrasoft pseudopotentials and zeroth-order regular approximation (ZORA) relativistic effects. An initial assessment was performed on each structure to determine a starting Monkhorst-Pack grid of n × n × n *k*-points, which was stepped iteratively at fine basis set precision (295 eV plane wave cut-off energy) until convergence of shielding parameters was reached (within ≈ 1 ppm). This *k*-point grid size was then used to compute the shielding + EFG tensor at increasing basis set precision until convergence was reached again. A Monkhorst-Pack grid of n × n × n *k*-points (n = 12 for SS $CsSnBr_3$, n = 14 for MCS $CsGeBr_3$, and n = 18 for MCS $CsSnBr_3$ and SS $CsGeBr_3$; and an extreme basis set precision (corresponding to a plane wave cutoff energy of 566 eV for $CsGeBr_3$ and 392 eV for $CsSnBr_3$) was applied to all computations. Magnetic shielding values converged to $\Delta\sigma^{calc} \leq 1$ ppm between increases in the k-point grid dimension parameter, n. Results are summarized in Tables S7-S12.

Diffuse reflectance spectroscopy

Diffuse reflectance spectra of ground samples were collected on a Cary 5000 UV-Vis-NIR spectrophotometer, equipped with a diffuse reflectance integrating sphere attachment. Samples were scanned at 600 nm/min from 3000 to 200 nm. The detector and grating filters were changed at 900 nm.

Optical band gaps were extracted by transforming reflectance data using the Kubelka-Munk function and fitting to Tauc plots.[19]

Raman spectroscopy

Raman spectra were collected from ground samples placed on a glass slide using a Renishaw inVia Raman microscope equipped with a 633 nm diode laser operating at 50 mW. At least three spots were measured for each sample, with an integration of 10 scans on each spot with 10% laser power.

Scanning electron microscopy and energy dispersive X-ray spectroscopy

The SS- and MCS-prepared samples were examined by scanning electron microscopy performed on a Zeiss Sigma field emission scanning electron microscope operated at an accelerating voltage of 5–20 kV and equipped with secondary and backscattered electron detectors, an in-lens detector, and an energy dispersive X-ray (EDX) spectrometer. Ground samples were placed on carbon tape on an aluminum stub. EDX analysis was performed with the Oxford Aztec software. The HT-prepared samples were also examined in a similar way, on a Zeiss Sigma 300 VP field emission scanning electron microscope operated with an accelerating voltage of 15 kV and equipped with a Bruker Quantax 600 system with dual X-Flash 6/60 detectors. Representative elemental maps are shown in Figures S10–S22, and EDX analyses are summarized in Table S6.

EPR spectroscopy

The EPR spectrum of HT-prepared $CsSnBr_3$ was recorded at room temperature using a Bruker EMX Nano spectrometer with X-band microwaves using an applied frequency of 9.626 GHz and a microwave attenuation of 25 dB under ambient conditions. The field modulation was 6 G at 100 kHz. Data were collected over 32 scans with a receiver gain of 35 dB. Microwave power was set at 0.3 mW, with the magnetic field centred at 3435 G, a sweep width of 500 G, and a sweep time of 60 seconds per scan. The experimental EPR spectrum was fit using the EasySpin simulation package.[20]

Rietveld refinements

$CsSn_xGe_{1-x}Br_3$ (SS)

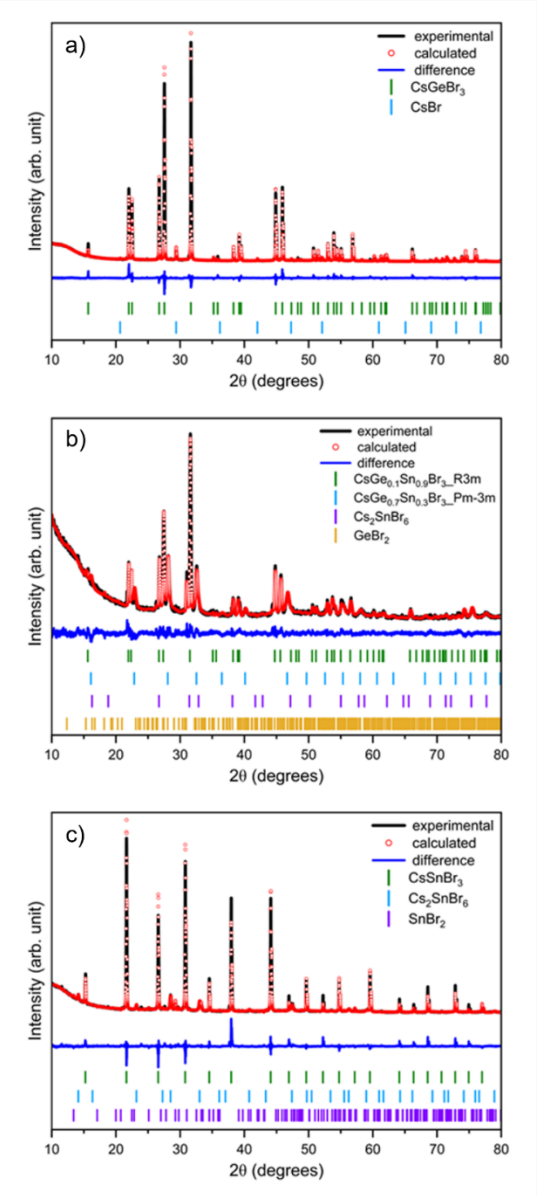

Figure S1. Rietveld refinements of SS-prepared $CsSn_xGe_{1-x}Br_3$ (x = 0, 0.50, 1).

$CsSn_xGe_{1-x}Br_3$ (MCS)

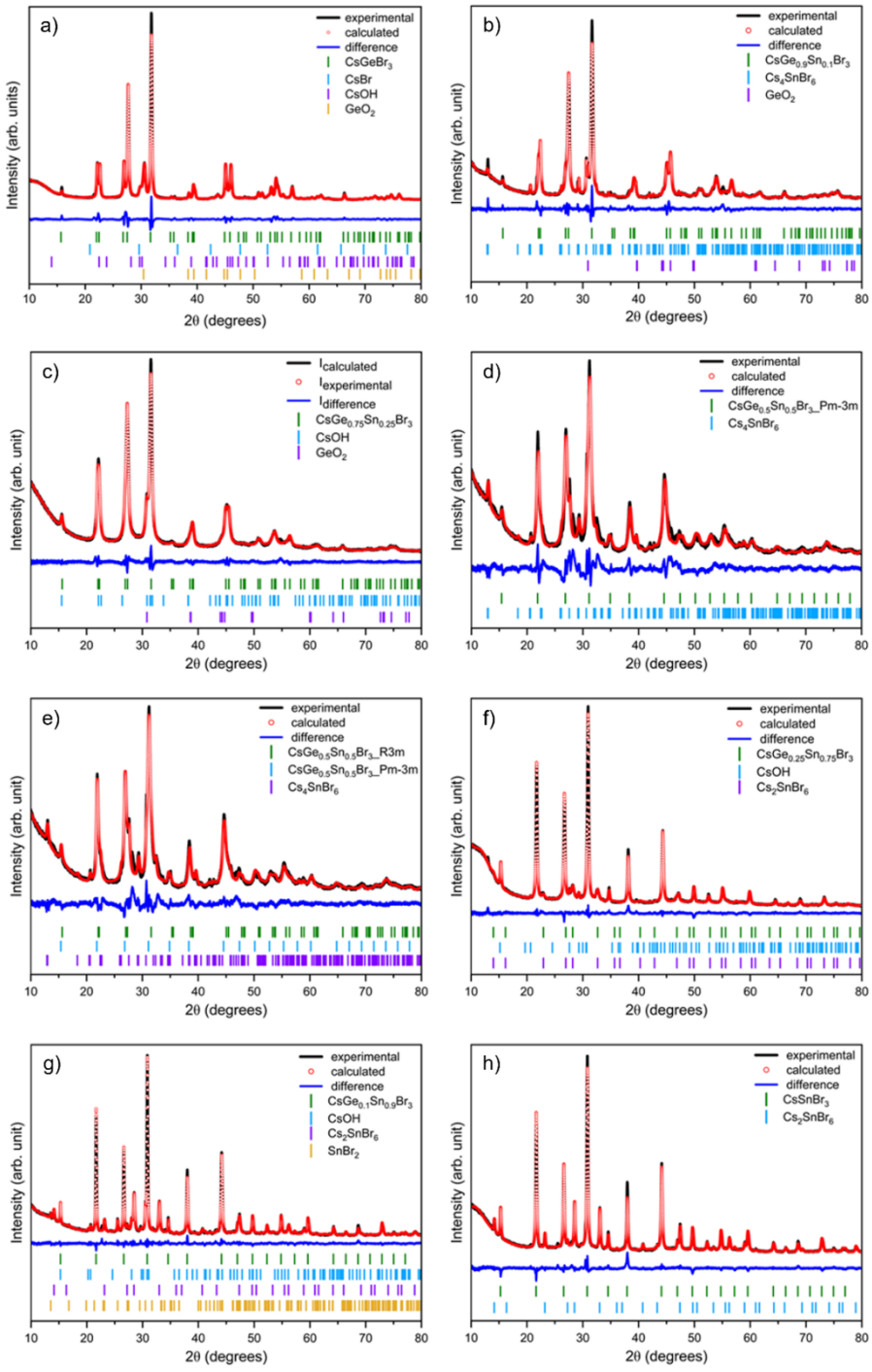

Figure S2. Rietveld refinements of MCS-prepared $CsSn_xGe_{1-x}Br_3$ (x = 0–1). Refinement in (d) is carried out only using a cubic model for the main phase, where (e) uses trigonal and cubic models for the main phase, as shown in Table S1.

$CsSn_xGe_{1-x}Br_3$ (HT)

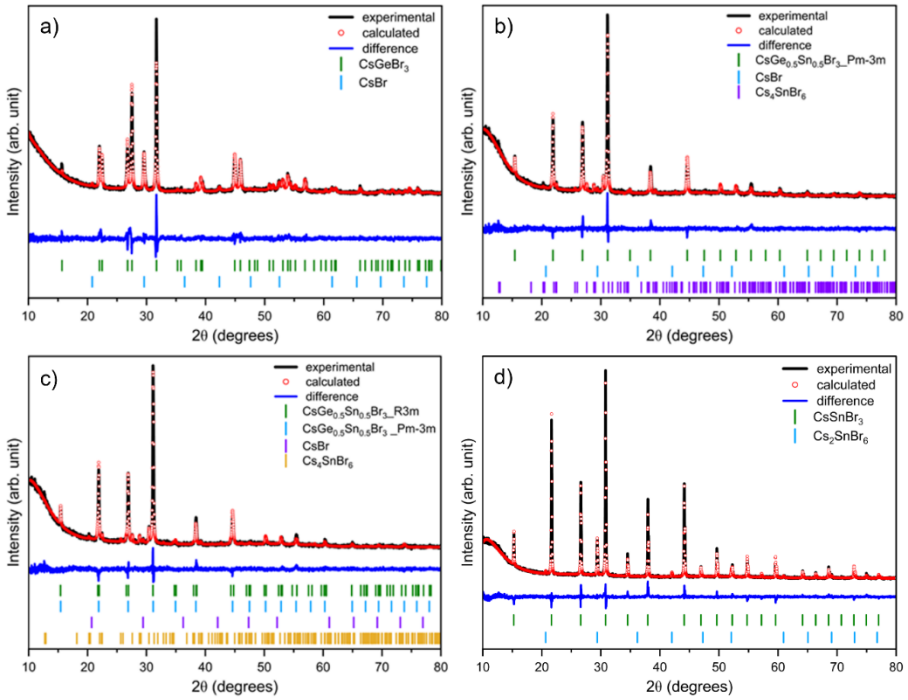

Figure S3. Rietveld refinements of HT-prepared $CsSn_xGe_{1-x}Br_3$ (x = 0, 0.50, 1).

Table S1. Cell parameters and refinement agreement factors for $CsSn_xGe_{1-x}Br_3$ (x = 0–1) samples.

Sample	a (Å)	c (Å)	R_p	R_{wp}
SS				
$CsGeBr_3$ $R3m$	7.89922	9.99789	4.26	6.45
$CsSn_{0.5}Ge_{0.5}Br_3$			3.56	4.84
$R3m$	7.95275	10.00776		
$Pm\bar{3}m$	5.50100	= a		
$CsSnBr_3$ $Pm\bar{3}m$	5.80348	= a	4.48	7.13
MCS				
$CsGeBr_3$ $R3m$	7.90974	9.98301	4.19	6.04
$CsSn_{0.1}Ge_{0.9}Br_3$ $R3m$	7.94072	9.92797	3.48	4.13
$CsSn_{0.25}Ge_{0.75}Br_3$ $R3m$	7.96923	9.9208	2.73	3.56
$CsSn_{0.5}Ge_{0.5}Br_3$			3.41	4.36
$R3m$	7.9747	9.88824		
$Pm\bar{3}m$	5.7495	= a		
$CsSn_{0.5}Ge_{0.5}Br_3$ $Pm\bar{3}m$ only	5.7451	= a	5.65	7.80[a]
$CsSn_{0.75}Ge_{0.25}Br_3$ $Pm\bar{3}m$	5.77437	= a	2.69	3.79
$CsSn_{0.9}Ge_{0.1}Br_3$ $Pm\bar{3}m$	5.7960	= a	3.16	4.24
$CsSnBr_3$ $Pm\bar{3}m$	5.80394	= a	3.41	4.92
HT				
$CsGeBr_3$ $R3m$	7.90508	9.97583	6.60	9.04
$CsSn_{0.5}Ge_{0.5}Br_3$			5.92	7.81
$R3m$	8.08496	10.05138		
$Pm\bar{3}m$	5.73907	= a		
$CsSn_{0.5}Ge_{0.5}Br_3$ $Pm\bar{3}m$ only	5.73843	= a	6.08	8.04
$CsSnBr_3$ $Pm\bar{3}m$	5.80234	= a	5.97	7.81

Table S2. Relative amounts of phases (wt. %) in $CsSn_xGe_{1-x}Br_3$ (x = 0–1) samples.

Sample	$CsSn_xGe_{1-x}Br_3$		CsBr	CsOH	Cs_2SnBr_6 or Cs_4SnBr_6	$(Sn,Ge)Br_2$	$(Sn,Ge)O_2$
	$R3m$	$Pm\bar{3}m$					
SS							
$CsGeBr_3$	97.8		2.2				
$CsSn_{0.5}Ge_{0.5}Br_3$	43.3	42.2			5.2	9.2	
$CsSnBr_3$		83.1			10.7	6.3	
MCS							
$CsGeBr_3$	77.0		1.8	7.8			13.4
$CsSn_{0.1}Ge_{0.9}Br_3$	86.6				8.3		5.1
$CsSn_{0.25}Ge_{0.75}Br_3$	88.1			1.1			10.8
$CsSn_{0.5}Ge_{0.5}Br_3$							
R3m and ***Pm$\bar{3}$m***	27.3	53.3			19.4		
Pm$\bar{3}$m only		80.4			19.6		
$CsSn_{0.75}Ge_{0.25}Br_3$		84.7		3.5	11.8		
$CsSn_{0.9}Ge_{0.1}Br_3$		64.5		12.4	19.4		3.6
$CsSnBr_3$		82.3			17.7		
HT							
$CsGeBr_3$	90.6		9.4				
$CsSn_{0.5}Ge_{0.5}Br_3$							
R3m and ***Pm$\bar{3}$m***	23.6	68.0	1.6		6.8		
Pm$\bar{3}$m only		92.8	1.3		6.0		
$CsSnBr_3$		93.7	6.3				

SCXRD

Table S3. Crystal data for $CsSn_{0.5}Ge_{0.5}Br_3$ from HT synthesis.

	crystal 1		crystal 2	
refined composition	$CsSn_{0.57}Ge_{0.43}Br_3$	$CsSn_{0.56}Ge_{0.44}Br_3$	$CsSn_{0.58}Ge_{0.42}Br_3$	$CsSn_{0.61}Ge_{0.39}Br_3$
formula mass (amu)	468.28	468.28	468.28	468.28
space group	$R3m$	$Pm\bar{3}m$	$R3m$	$Pm\bar{3}m$
a (Å)	8.080(15)	5.699(11)	8.111(3)	5.7357(15)
c (Å)	9.883(18)	= a	9.933(5)	= a
V (Å^3)	559(2)	185(1)	566.0(4)	188.7(2)
Z	3	1	3	1
T (K)	296(2)	296(2)	296(2)	296(2)
ρ_{calcd} (g cm^{-3})	4.174	4.202	4.122	4.121
μ(Mo $K\alpha$) (mm^{-1})	24.55	24.71	24.24	24.23
transmission factors	0.293–0.433	0.307–0.433	0.334–0.433	0.333–0.433
2θ limits	7.13–61.28	7.15–60.88	7.10–60.95	7.10–60.95
data collected	$-11 \le h \le 11$, $-11 \le k \le 11$, $-14 \le l \le 14$	$-8 \le h \le 8$, $-8 \le k \le 8$, $-8 \le l \le 8$	$-11 \le h \le 11$, $-11 \le k \le 11$, $-14 \le l \le 14$	$-8 \le h \le 8$, $-8 \le k \le 8$, $-8 \le l \le 8$
no. of data collected	4919	4883	4948	4948
no. of unique data, including $F_o^2 < 0$	465 (R_{int} = 0.114)	85 (R_{int} = 0.105)	465 (R_{int} = 0.125)	86 (R_{int} = 0.131)
no. of unique data, with $F_o^2 > 2\sigma(F_o^2)$	246	57	251	58
no. of variables	14	7	15	7
$R(F)$ for $F_o^2 > 2\sigma(F_o^2)$ [a]	0.043	0.031	0.044	0.030
$R_w(F_o^2)$ [b]	0.114	0.097	0.071	0.061
goodness of fit	0.99	1.05	0.98	1.13
$(\Delta\rho)_{max}$, $(\Delta\rho)_{min}$ (e Å^{-3})	2.28, –0.85	1.90, –0.56	0.76, –0.85	0.54, –0.66

[a] $R(F) = \sum||F_o| - |F_c|| / \sum|F_o|$. [b] $R_w(F_o^2) = [\sum[w(F_o^2 - F_c^2)^2] / \sum wF_o^4]^{1/2}$; $w^{-1} = [\sigma^2(F_o^2) + (Ap)^2 + Bp]$, where $p = [\max(F_o^2,0) + 2F_c^2] / 3$.

Table S4. Atomic coordinates and equivalent isotropic displacement parameters for $CsSn_{0.5}Ge_{0.5}Br_3$.

atom	Wyckoff position	occupancy	*x*	*y*	*z*	U_{eq} (Å^2) [a]
crystal 1						
$R3m$						
Cs	3*a*	1	0	0	0.503(4)	0.081(1)
Tt	3*a*	0.57(3) Sn, 0.43(3) Ge	0	0	0.0	0.046(1)
Br	9*b*	1	0.502(2)	0.498(2)	0.508(5)	0.100(1)
$Pm\bar{3}m$						
Cs	1*b*	1	½	½	½	0.082(1)
Tt	1*a*	0.56(4) Sn, 0.44(4) Ge	0	0	0	0.047(1)
Br	3*d*	1	½	0	0	0.100(1)
crystal 2						
$R3m$						
Cs	3*a*	1	0	0	0.500(2)	0.078(1)
Tt	3*a*	0.58(2) Sn, 0.42(2) Ge	0	0	0.0	0.040(1)
Br	9*b*	1	0.504(1)	0.496(1)	0.494(2)	0.094(1)
$Pm\bar{3}m$						
Cs	1*b*	1	½	½	½	0.079(1)
Tt	1*a*	0.61(2) Sn, 0.39(2) Ge	0	0	0	0.041(1)
Br	3*d*	1	½	0	0	0.095(1)

[a] U_{eq} is defined as one third of the trace of the orthogonalized U_{ij} tensor.

Table S5. Interatomic distances and ranges of Br–*Tt*–Br angles for $CsSn_{0.5}Ge_{0.5}Br_3$.

	Cs–Br (Å)	*Tt*–Br (Å)	range of Br–*Tt*–Br (°)
crystal 1			
$R3m$	3.99(5) ×3	2.82(3) ×3	88(1)–92(1)
	4.03(1) ×3	2.89(3) ×3	
	4.05(1) ×3		
	4.08(5) ×3		
$Pm\bar{3}m$	4.029(8) ×12	2.849(6) ×6	90
crystal 2			
$R3m$	4.04(2) ×3	2.79(1) ×3	89.5(6)–90.6(6)
	4.06(1) ×3	2.94(1) ×3	
	4.06(1) ×3		
	4.08(1) ×3		
$Pm\bar{3}m$	4.0561(1) ×12	2.8679(8) ×6	90

^{133}Cs T_1 data

$CsSn_xGe_{1-x}Br_3$ SS

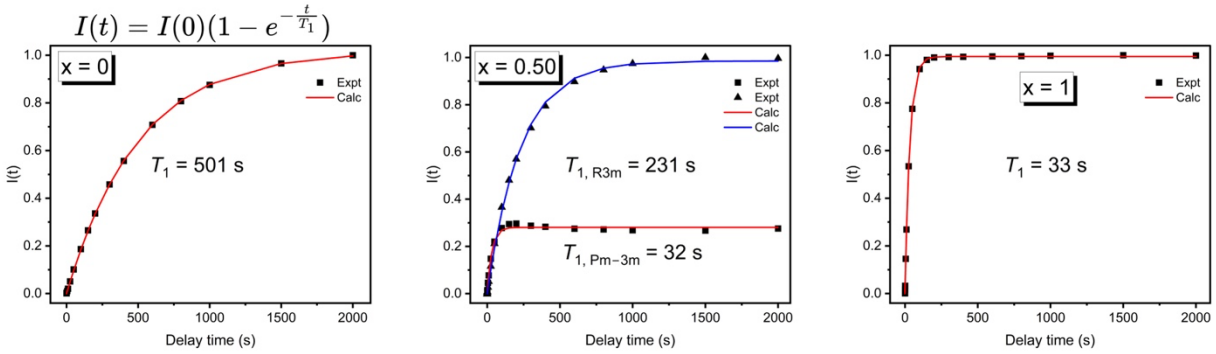

Figure S4. ^{133}Cs T_1 relaxation curves for SS series.

$CsSn_xGe_{1-x}Br_3$ MCS

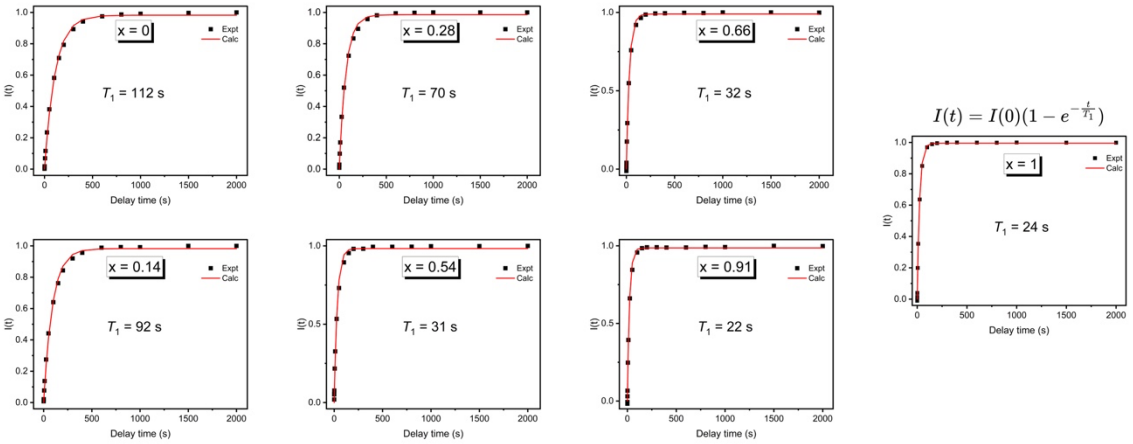

Figure S5. ^{133}Cs T_1 relaxation curves for MCS series.

$CsSn_xGe_{1-x}Br_3$ HT

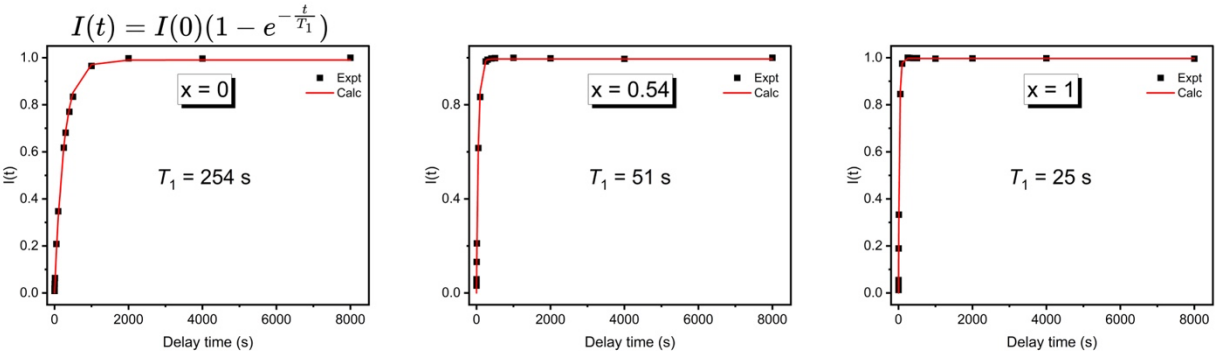

Figure S6. ^{133}Cs T_1 relaxation curves for HT series.

DRS plots

$CsSn_xGe_{1-x}Br_3$ SS

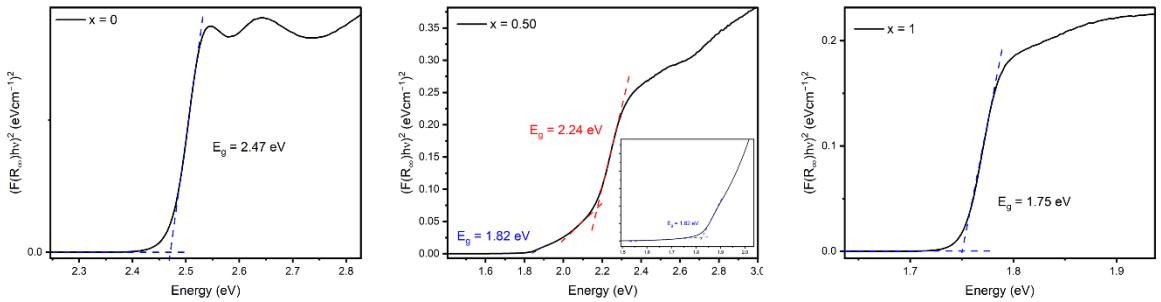

Figure S7. Optical bandgap Tauc plots for SS series.

$CsSn_xGe_{1-x}Br_3$ MCS

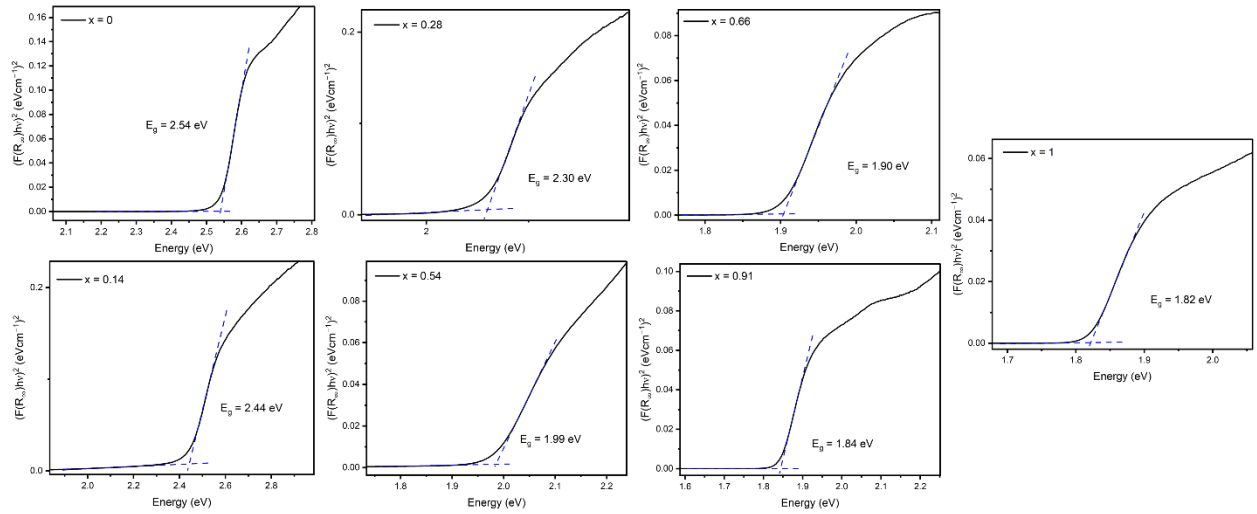

Figure S8. Optical bandgap Tauc plots for MCS series.

$CsSn_xGe_{1-x}Br_3$ HT

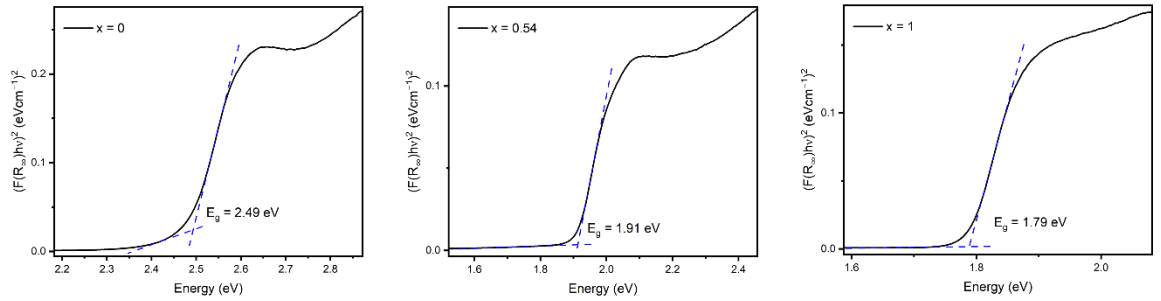

Figure S9. Optical bandgap Tauc plots for HT series.

EDX analysis

Table S6. Nominal and EDX-averaged compositions of $CsSn_xGe_{1-x}Br_3$ series.

Synthetic Route	Desired Compound	Cs Atom (%)		Sn Atom (%)		Ge Atom (%)		Br Atom (%)	
		Nominal	EDX Analysis	Nominal	EDX Analysis	Nominal	EDX Analysis	Nominal	EDX Analysis
MCS	$CsGeBr_3$	20	21.6	–	–	20	20.6	60	57.8
	$CsSn_{0.1}Ge_{0.9}Br_3$	20	20.4	2	2.8	18	16.8	60	60.1
	$CsSn_{0.25}Ge_{0.75}Br_3$	20	19.5	5	5.5	15	13.9	60	61.1
	$CsSn_{0.5}Ge_{0.5}Br_3$	20	20.8	10	10.2	10	8.7	60	60.3
	$CsSn_{0.75}Ge_{0.25}Br_3$	20	21.9	15	14.4	5	7.3	60	56.5
	$CsSn_{0.9}Ge_{0.1}Br_3$	20	20.5	18	18.5	2	1.9	60	59.1
	$CsSnBr_3$	20	20.9	20	20.8	–	–	60	58.3
SS	$CsGeBr_3$	20	19.1	–	–	20	28.7	60	52.3
	$CsSn_{0.5}Ge_{0.5}Br_3$	20	21	10	5.5	10	24.7	60	48.8
	$CsSnBr_3$	20	20.9	20	18.7	–	–	60	60.4
HTS	$CsGeBr_3$	20	19.5	–	–	20	19.0	60	61.4
	$CsSn_{0.5}Ge_{0.5}Br_3$	20	18.7	10	10.0	10	8.6	60	62.7
	$CsSnBr_3$	20	18.5	20	18.2	–	–	60	63.3

$CsSn_xGe_{1-x}Br_3$ SS

x = 0

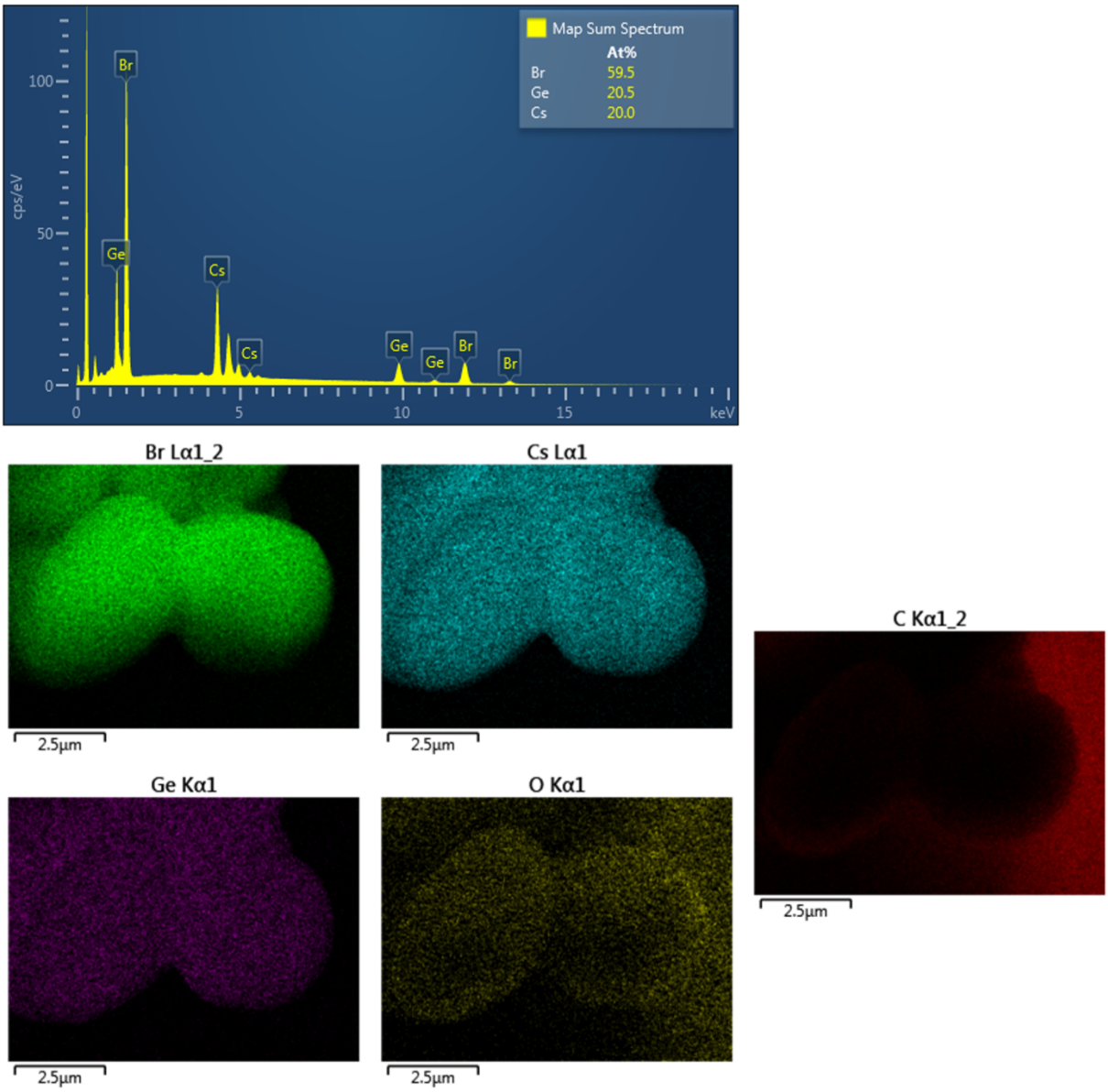

Figure S10. EDX analysis for SS $CsGeBr_3$.

x = 0.50

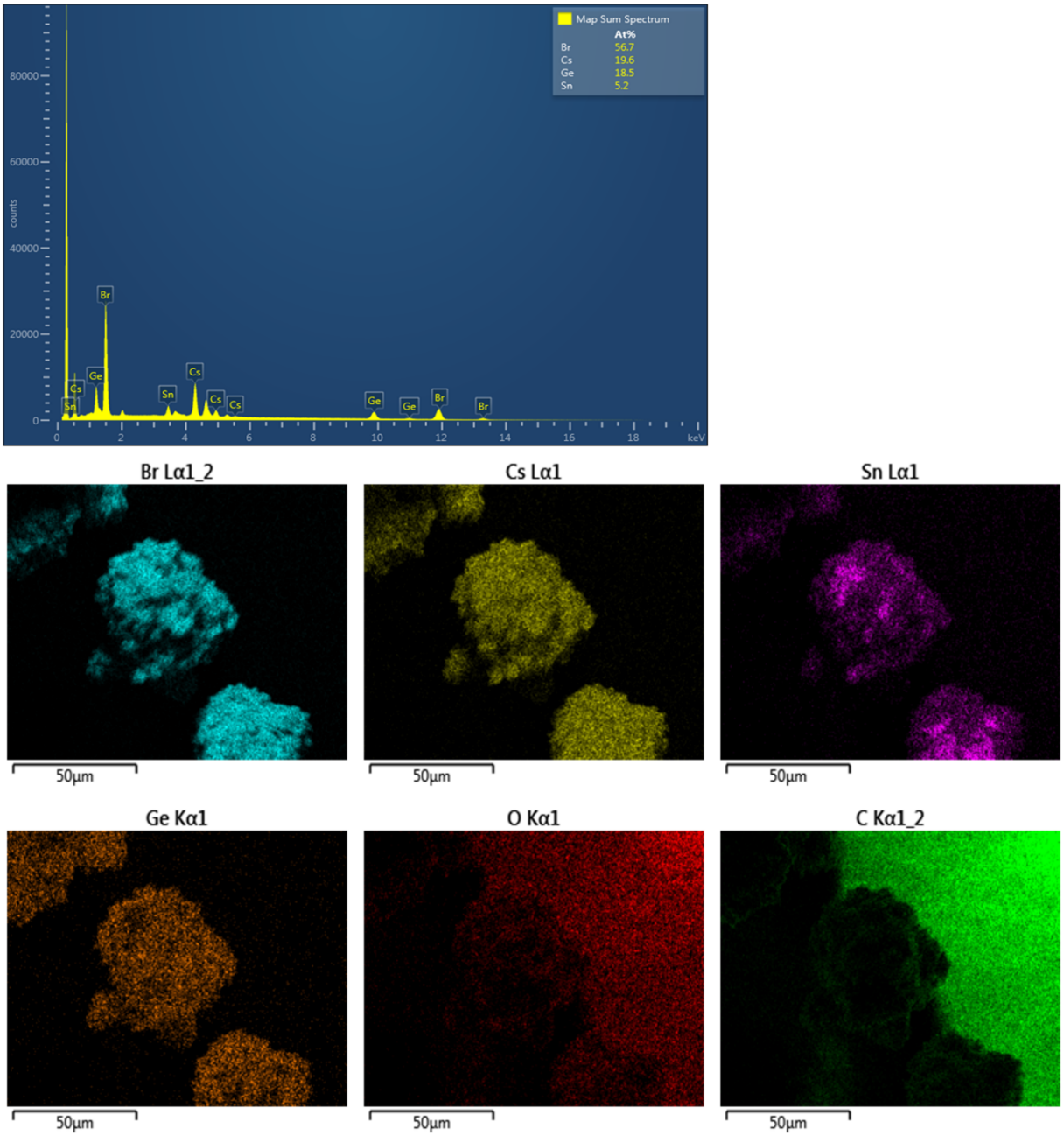

Figure S11. EDX analysis for SS $CsSn_{0.5}Ge_{0.5}Br_3$.

x = 1

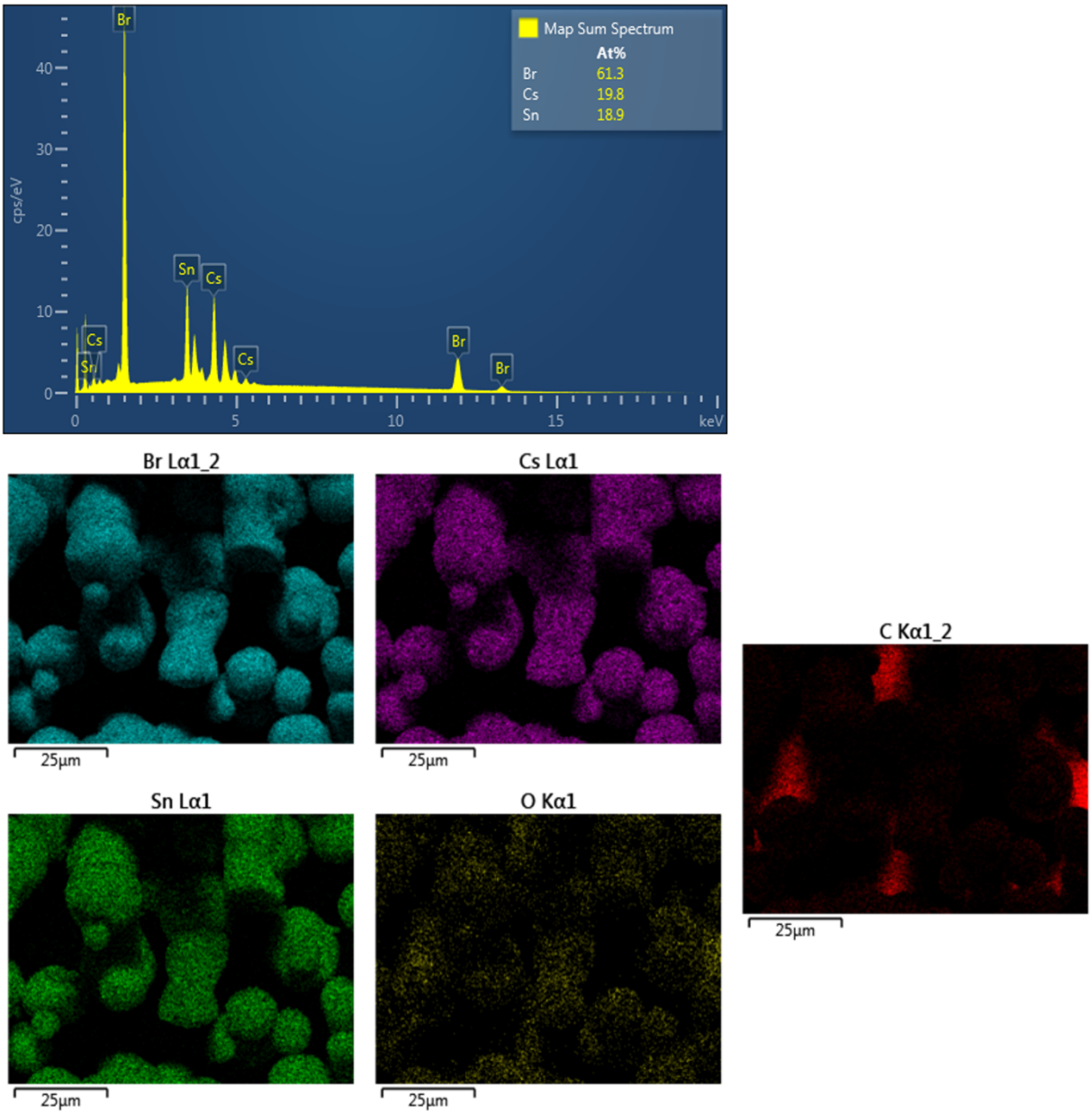

Figure S12. EDX analysis for SS $CsSnBr_3$.

$CsSn_xGe_{1-x}Br_3$ MCS

x = 0

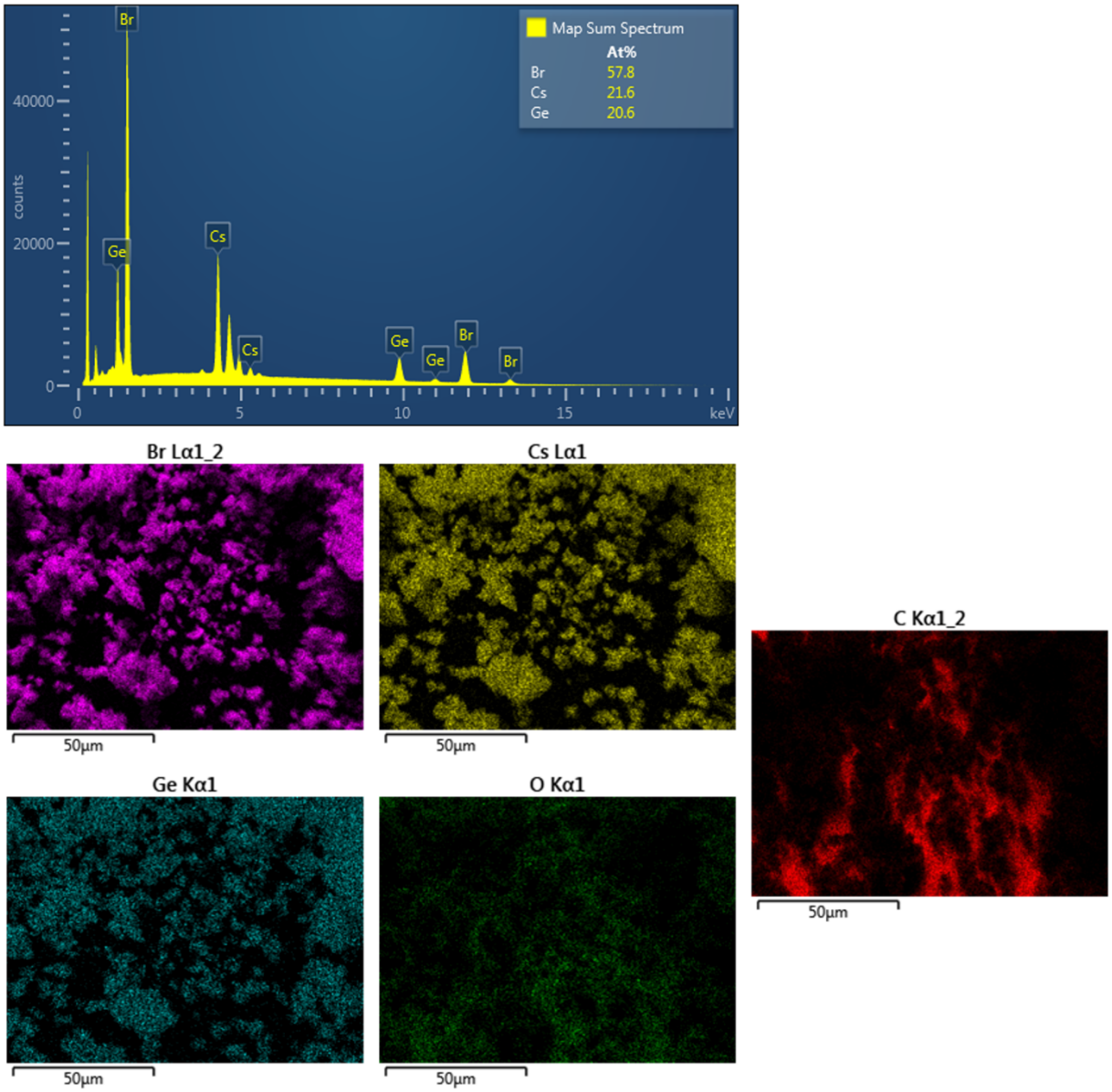

Figure S13. EDX analysis for MCS $CsGeBr_3$.

x = 0.10

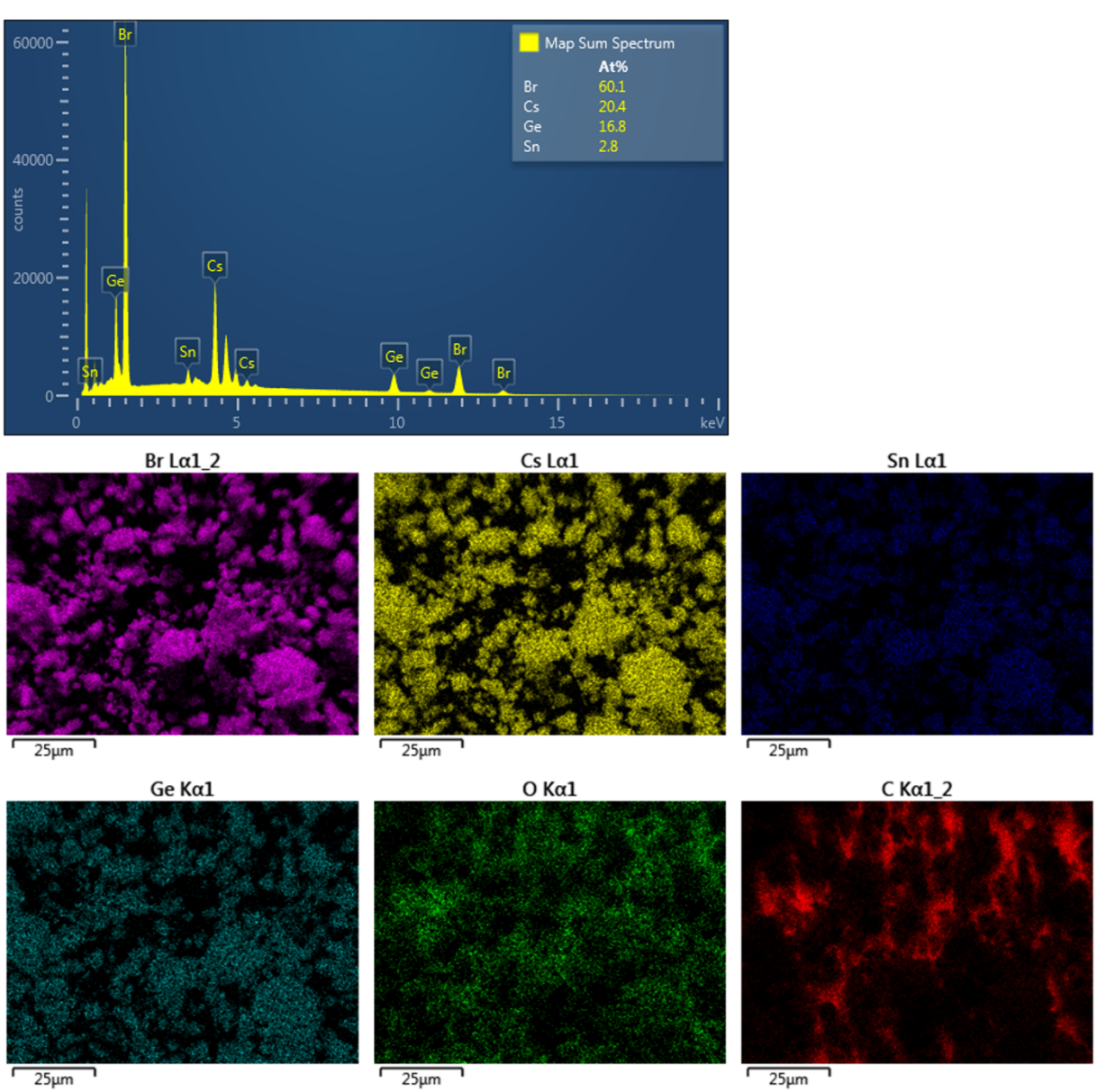

Figure S14. EDX analysis for MCS $CsSn_{0.1}Ge_{0.9}Br_3$.

x = 0.25

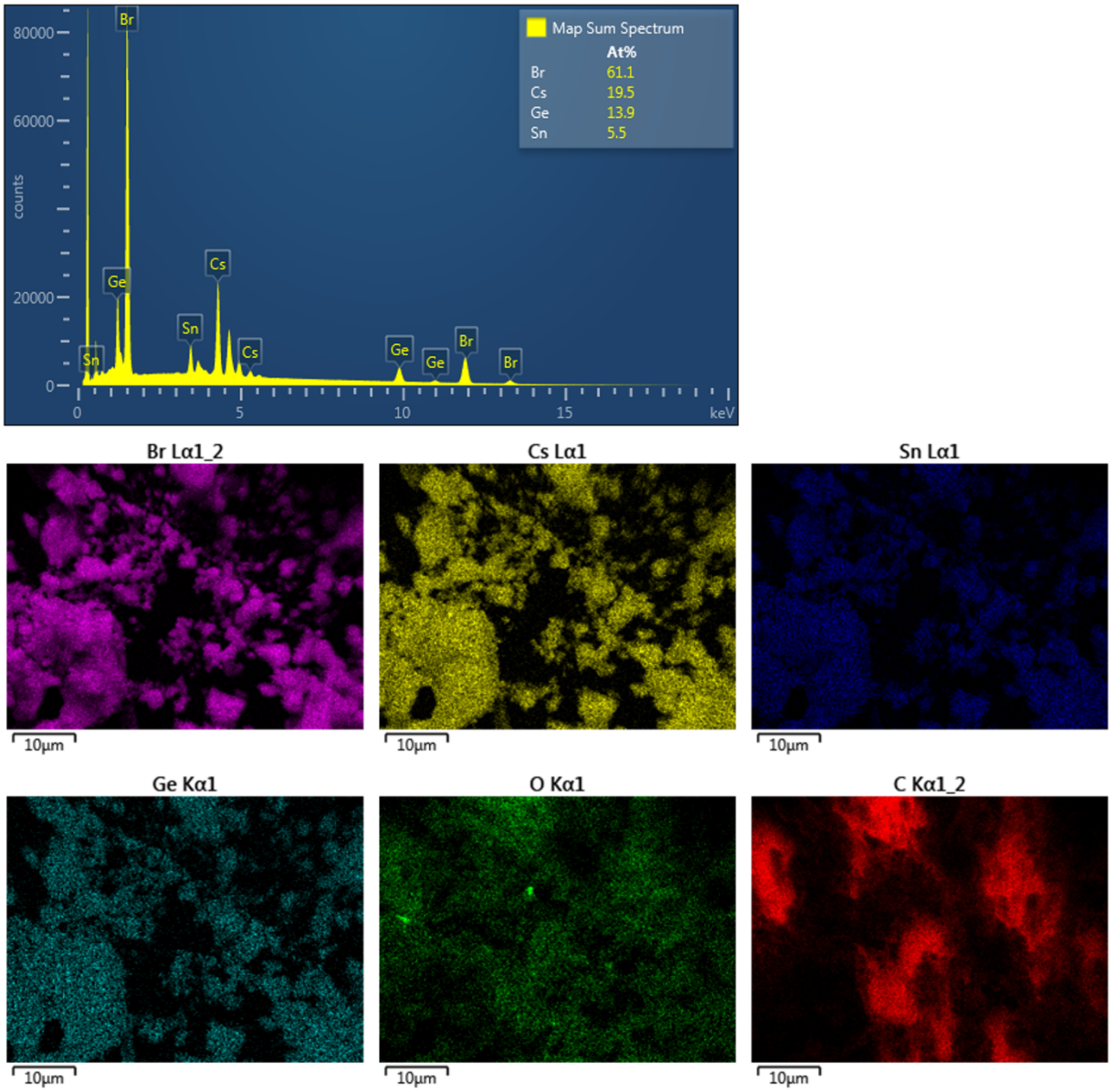

Figure S15. EDX analysis for MCS $CsSn_{0.25}Ge_{0.75}Br_3$.

x = 0.50

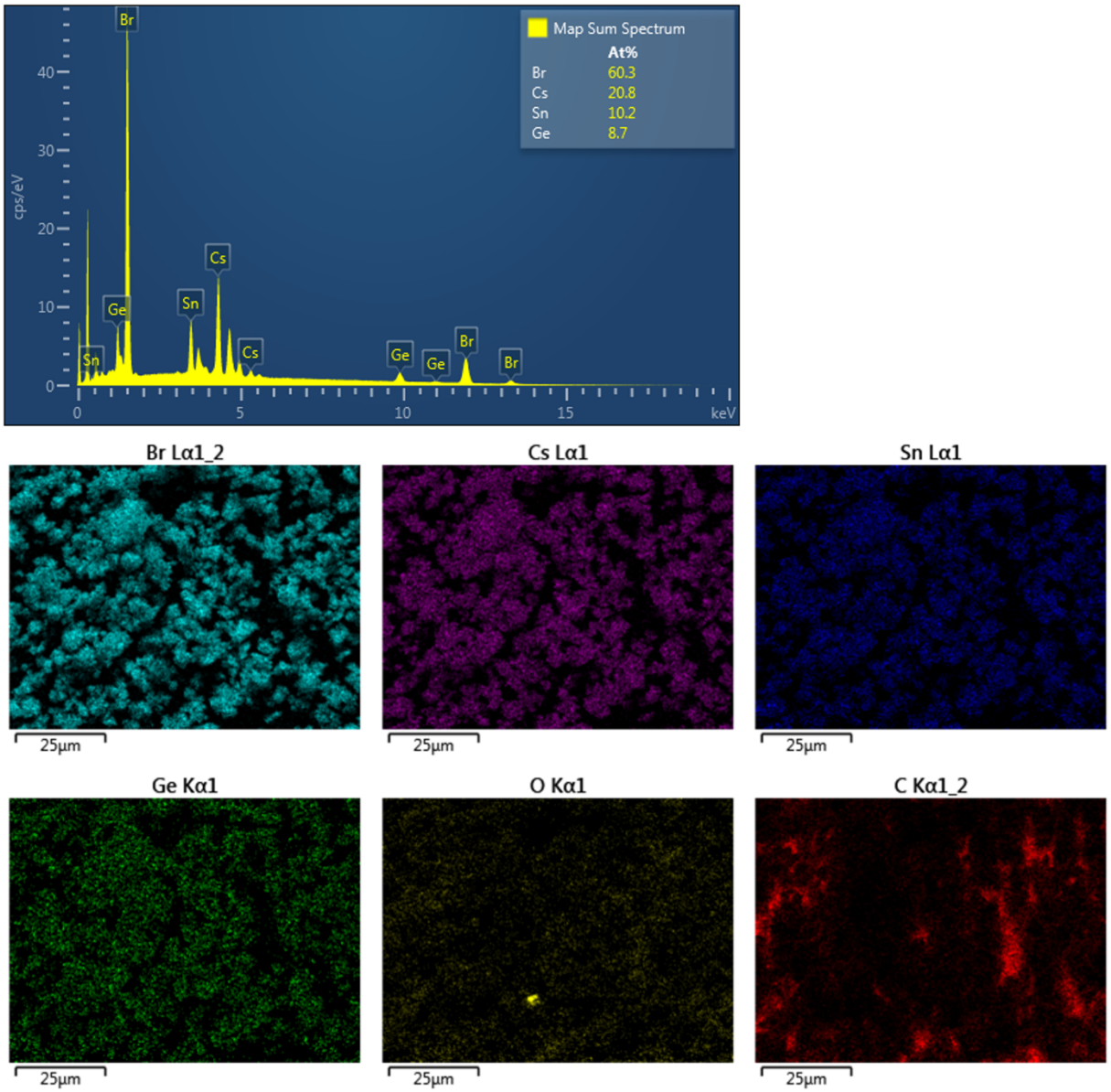

Figure S16. EDX analysis for MCS $CsSn_{0.5}Ge_{0.5}Br_3$.

x = 0.75

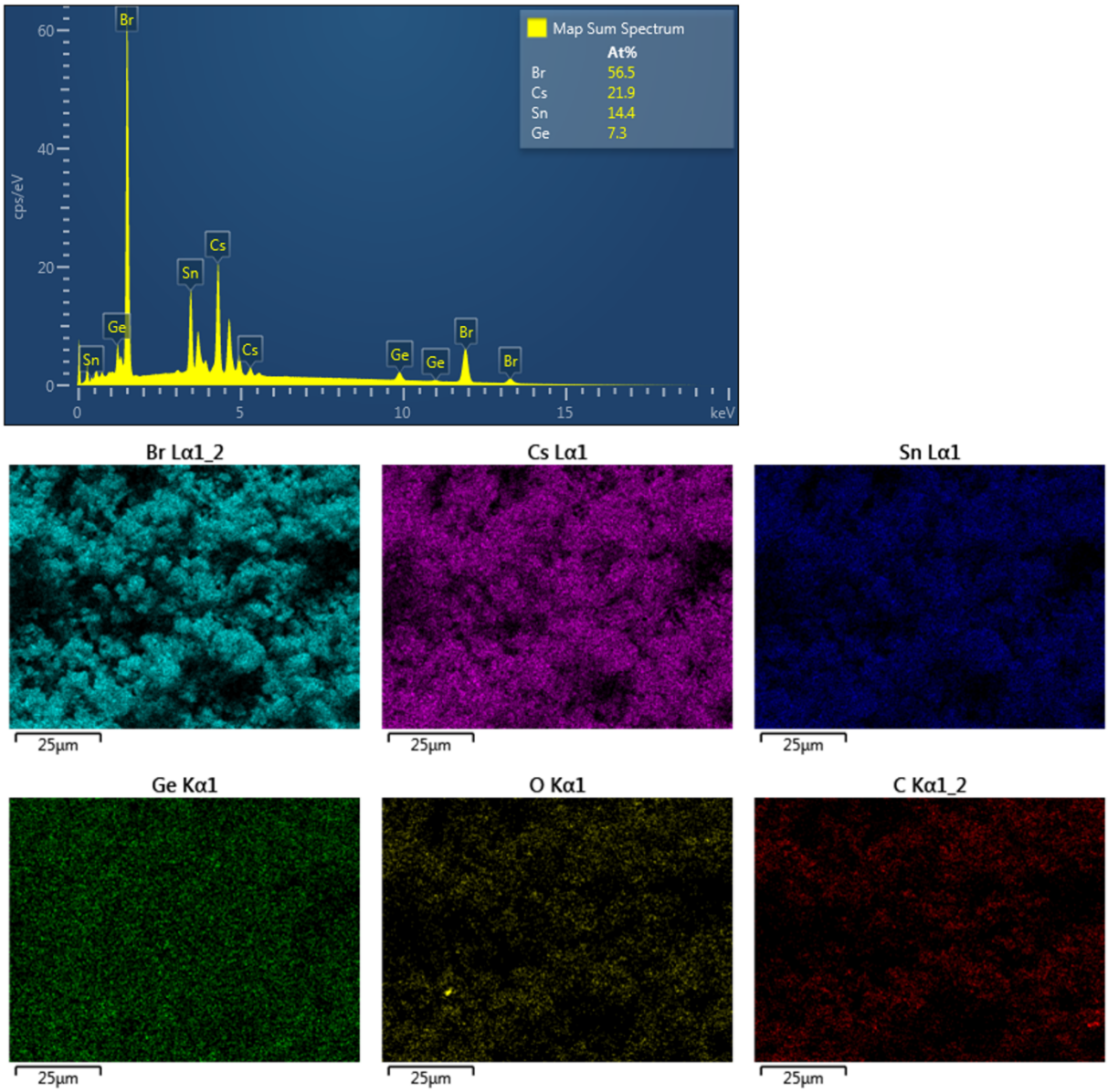

Figure S17. EDX analysis for MCS $CsSn_{0.75}Ge_{0.25}Br_3$.

x = 0.90

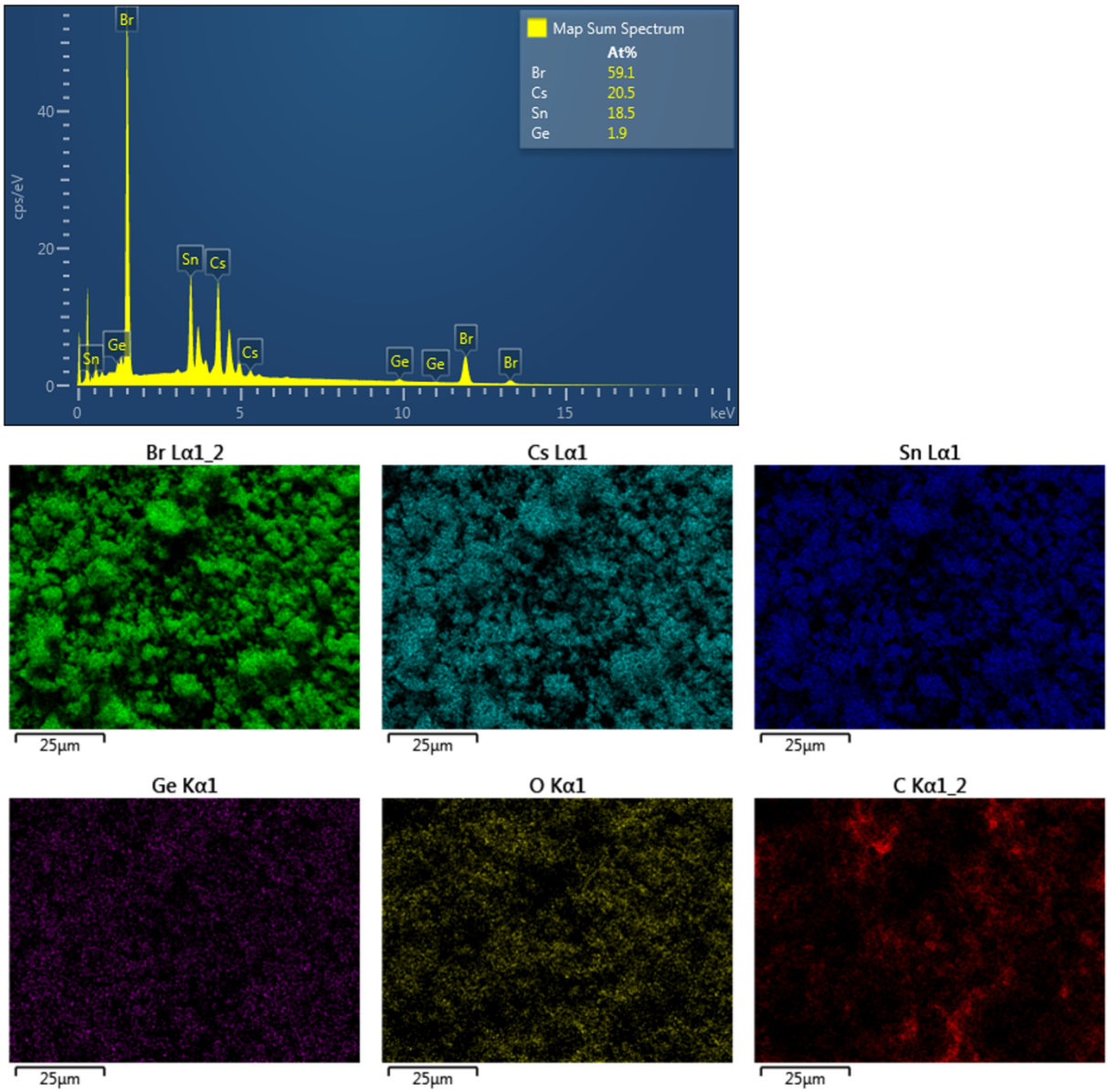

Figure S18. EDX analysis for MCS $CsSn_{0.9}Ge_{0.1}Br_3$.

x = 1

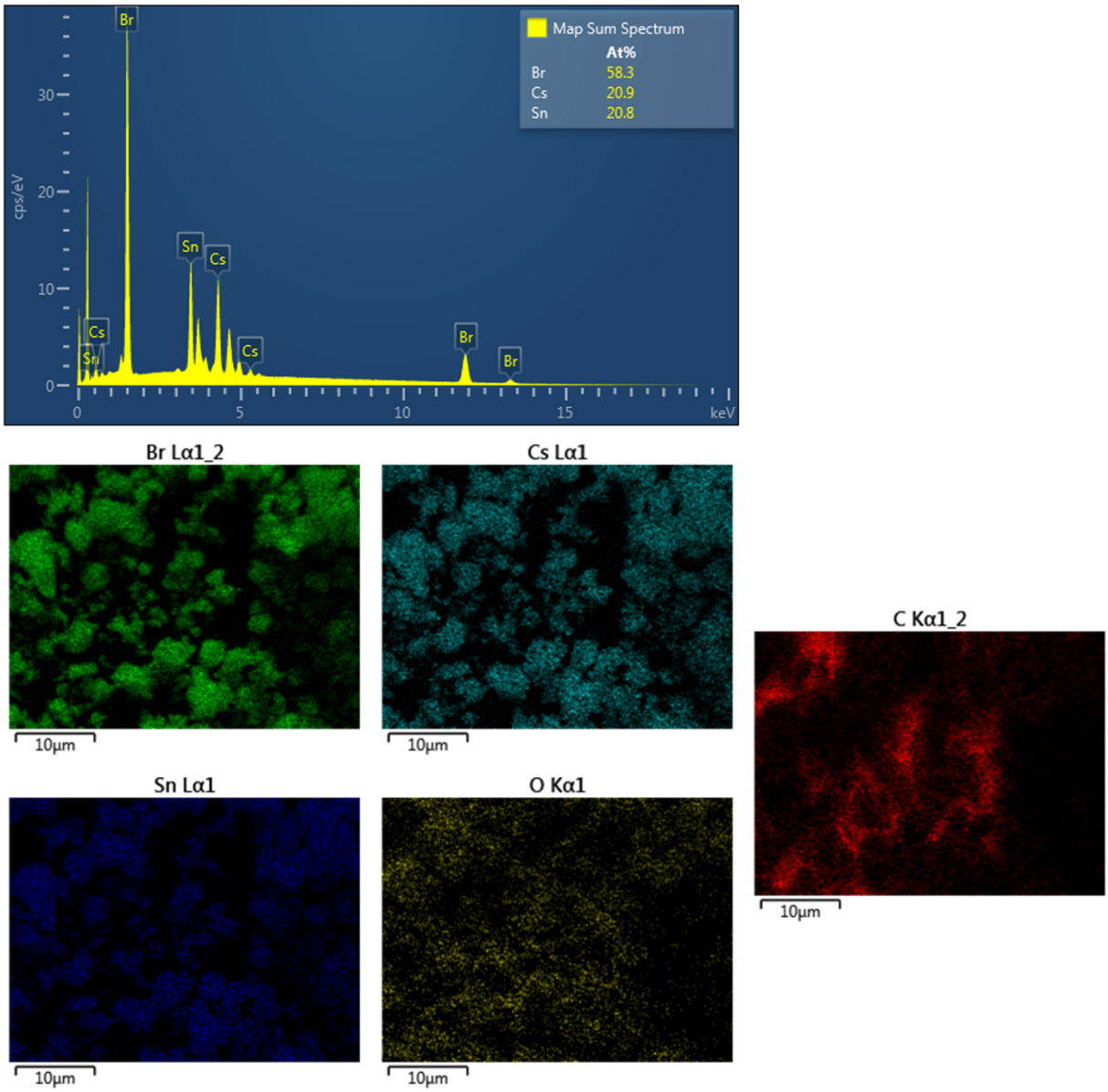

Figure S19. EDX analysis for MCS $CsSnBr_3$.

$CsSn_xGe_{1-x}Br_3$ HT

x = 0

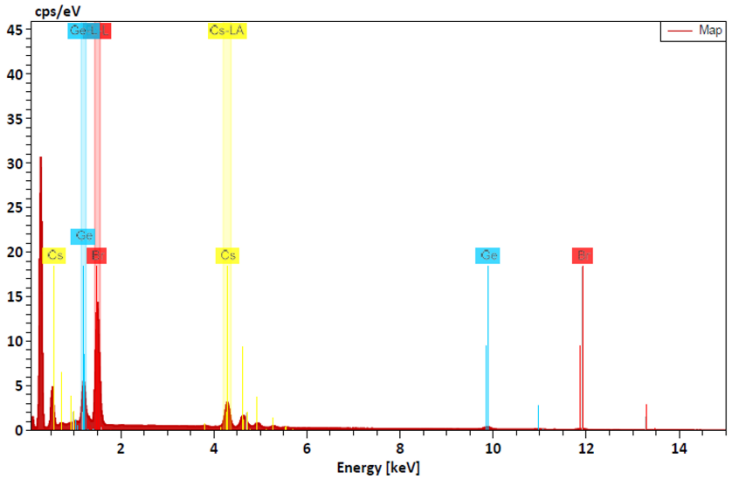

Map

Element	At. No.	Line s.	Netto	Mass [%]	Mass Norm. [%]	Atom [%]	abs. error [%] (1 sigma)	abs. error [%] (2 sigma)	abs. error [%] (3 sigma)
Germanium	32	L-Serie	82828	11.88	15.34	19.04	0.69	1.38	2.07
Bromine	35	L-Serie	286921	40.61	52.43	59.12	1.91	3.83	5.74
Cesium	55	L-Serie	124980	24.96	32.23	21.85	0.75	1.49	2.24
			Sum	**77.44**	**100.00**	**100.00**			

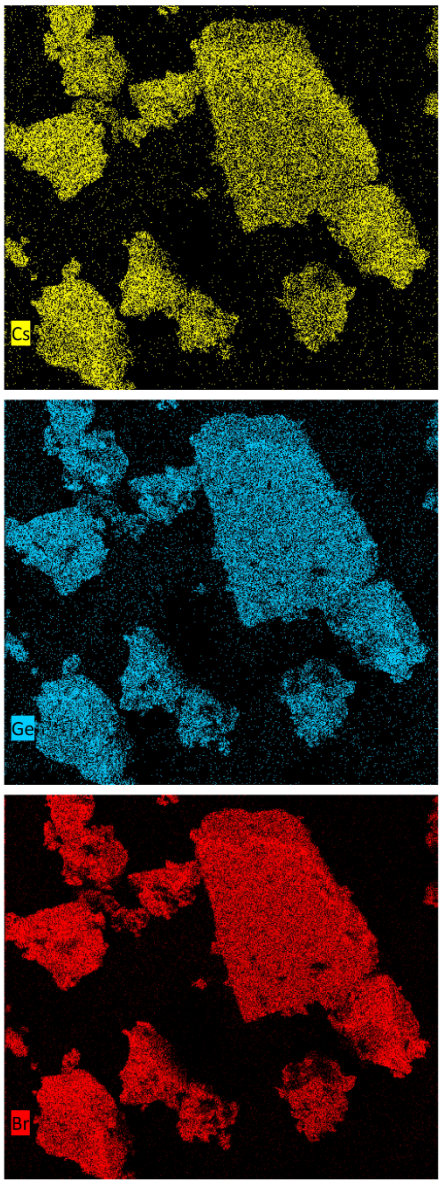

Figure S20. EDX analysis for HT $CsGeBr_3$.

x = 0.50

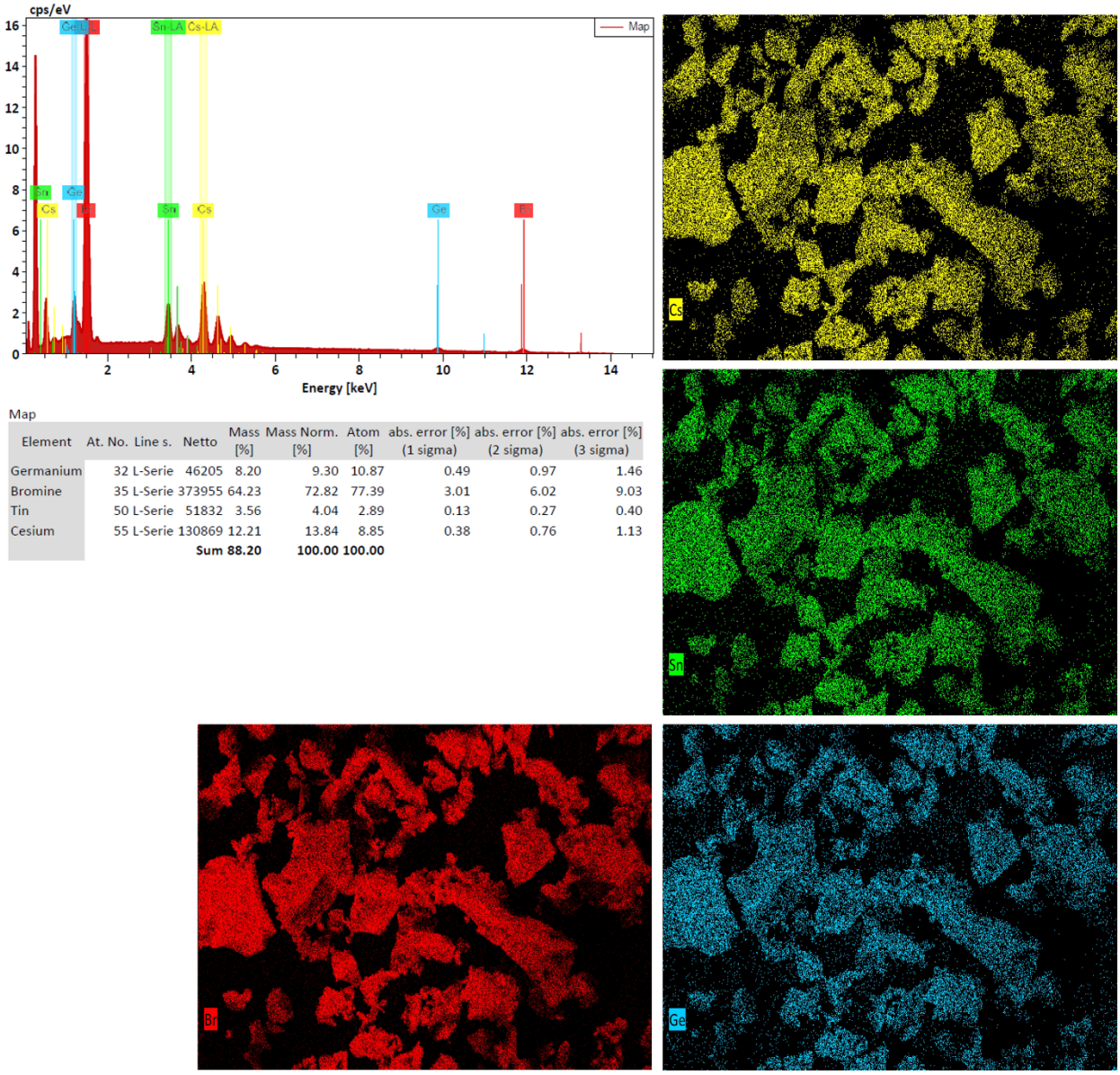

Map

Element	At. No.	Line s.	Netto	Mass [%]	Mass Norm. [%]	Atom [%]	abs. error [%] (1 sigma)	abs. error [%] (2 sigma)	abs. error [%] (3 sigma)
Germanium	32	L-Serie	46205	8.20	9.30	10.87	0.49	0.97	1.46
Bromine	35	L-Serie	373955	64.23	72.82	77.39	3.01	6.02	9.03
Tin	50	L-Serie	51832	3.56	4.04	2.89	0.13	0.27	0.40
Cesium	55	L-Serie	130869	12.21	13.84	8.85	0.38	0.76	1.13
			Sum	**88.20**	**100.00**	**100.00**			

Figure S21. EDX analysis for HT $CsSn_{0.5}Ge_{0.5}Br_3$.

x = 1

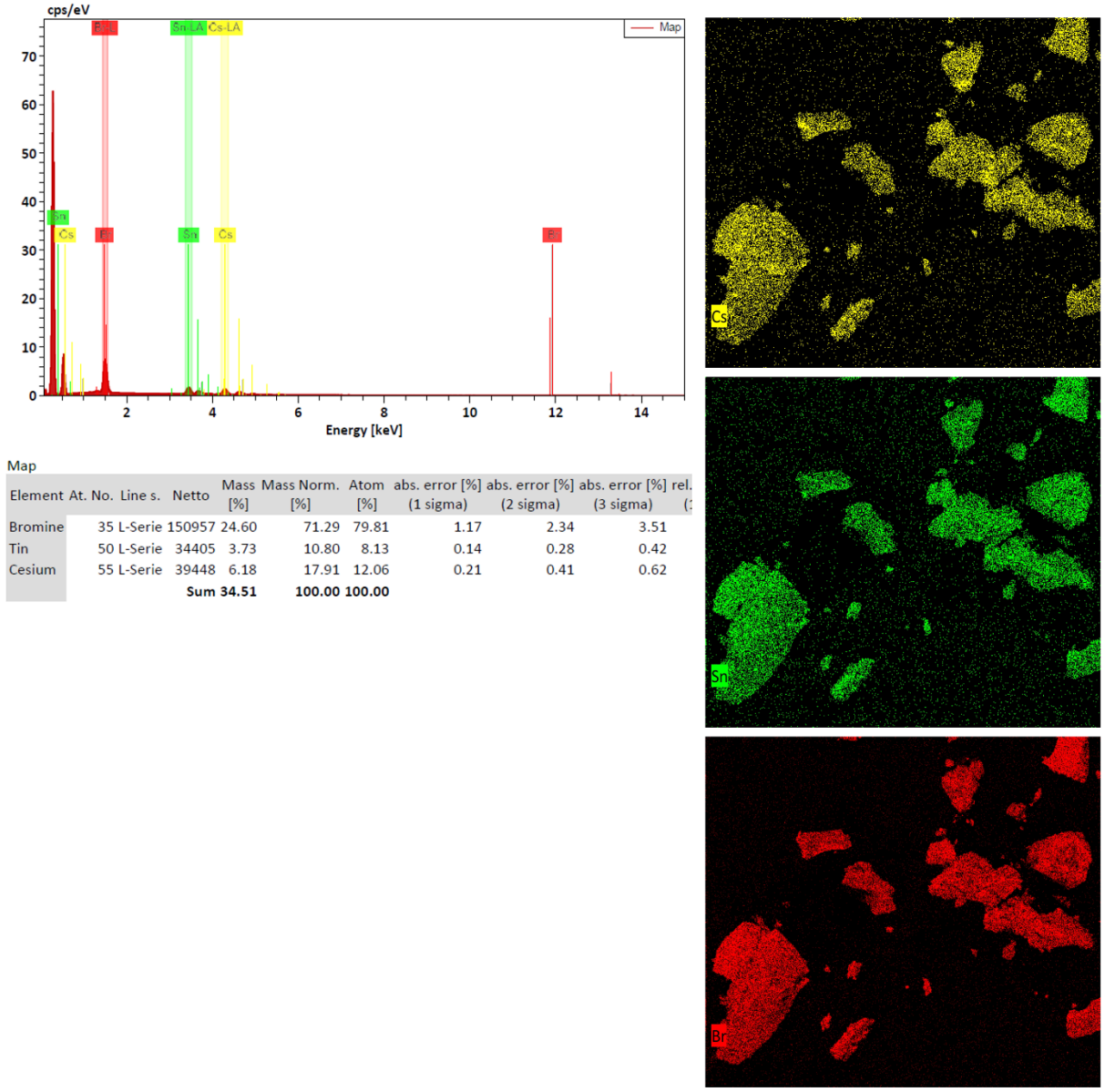

Map

Element	At. No.	Line s.	Netto	Mass [%]	Mass Norm. [%]	Atom [%]	abs. error [%] (1 sigma)	abs. error [%] (2 sigma)	abs. error [%] (3 sigma)	rel.
Bromine	35	L-Serie	150957	24.60	71.29	79.81	1.17	2.34	3.51	
Tin	50	L-Serie	34405	3.73	10.80	8.13	0.14	0.28	0.42	
Cesium	55	L-Serie	39448	6.18	17.91	12.06	0.21	0.41	0.62	
			Sum	**34.51**	**100.00**	**100.00**				

Figure S22. EDX analysis for HT $CsSnBr_3$.

Additional NMR spectra

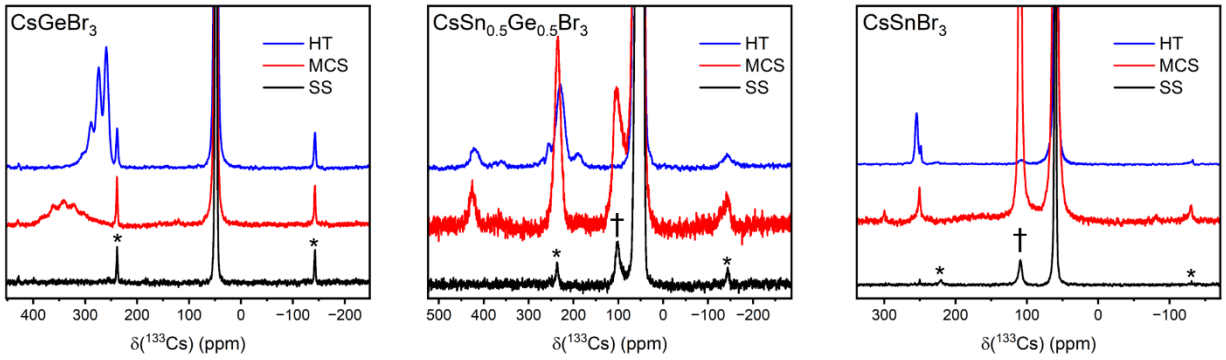

Figure S23. ^{133}Cs MAS NMR spectra for $CsGeBr_3$, $CsSn_{0.5}Ge_{0.5}Br_3$, and $CsSnBr_3$ (B_0 = 14.1 T, ν_r = 15 kHz) made *via* SS, MCS and HT. † denotes Cs_2BBr_6 impurity, * indicate spinning sidebands.

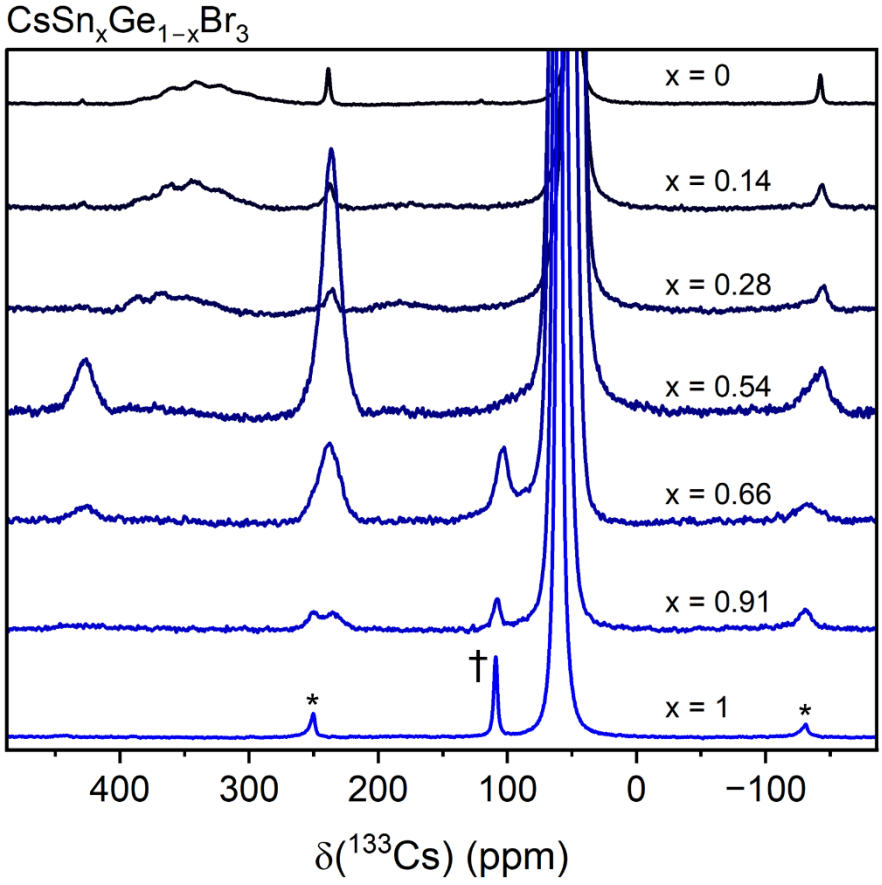

Figure S24. Enlarged ^{133}Cs MAS NMR spectra for MCS $CsSn_xGe_{1-x}Br_3$ (B_0 = 14.1 T, ν_r = 15 kHz). † denotes Cs_2BBr_6 impurity, * indicate spinning sidebands.

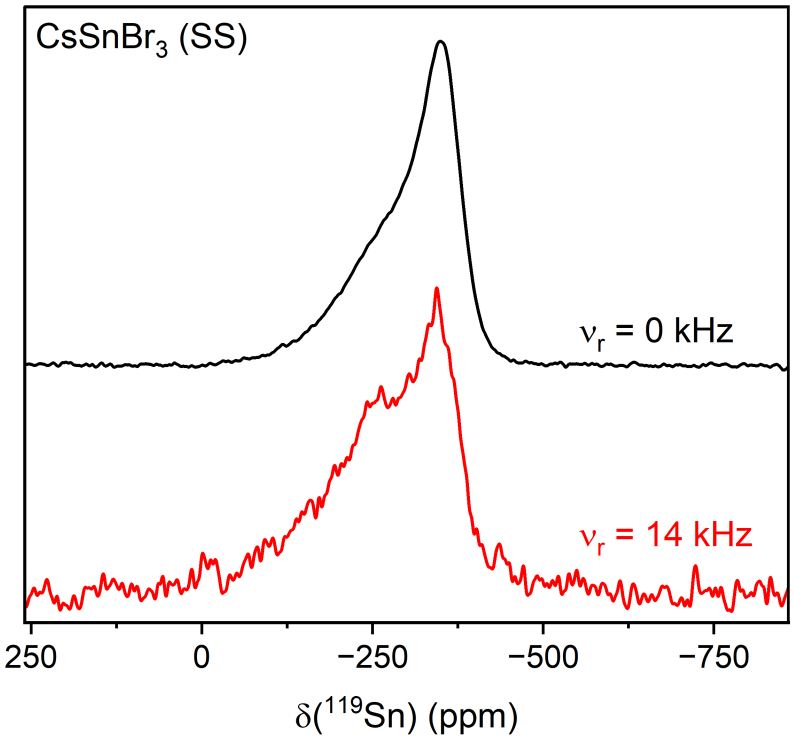

Figure S25. Non-spinning (black) and MAS (red) ^{119}Sn NMR for SS $CsSnBr_3$ (B_0 = 11.7 T).

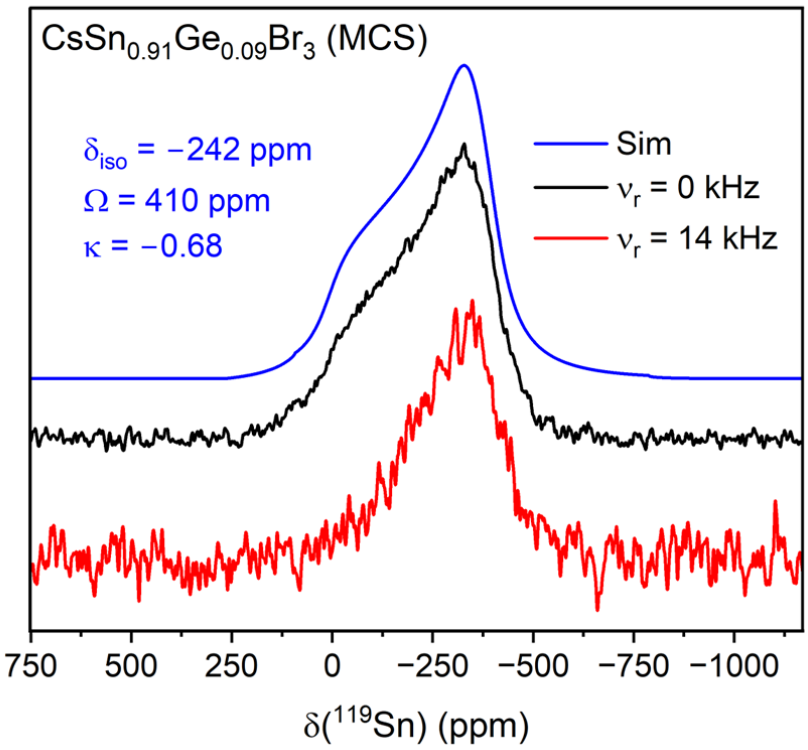

Figure S26. Non-spinning (black) and MAS (red) ^{119}Sn NMR for MCS $CsSn_{0.91}Ge_{0.09}Br_3$ (B_0 = 11.7 T).

EPR

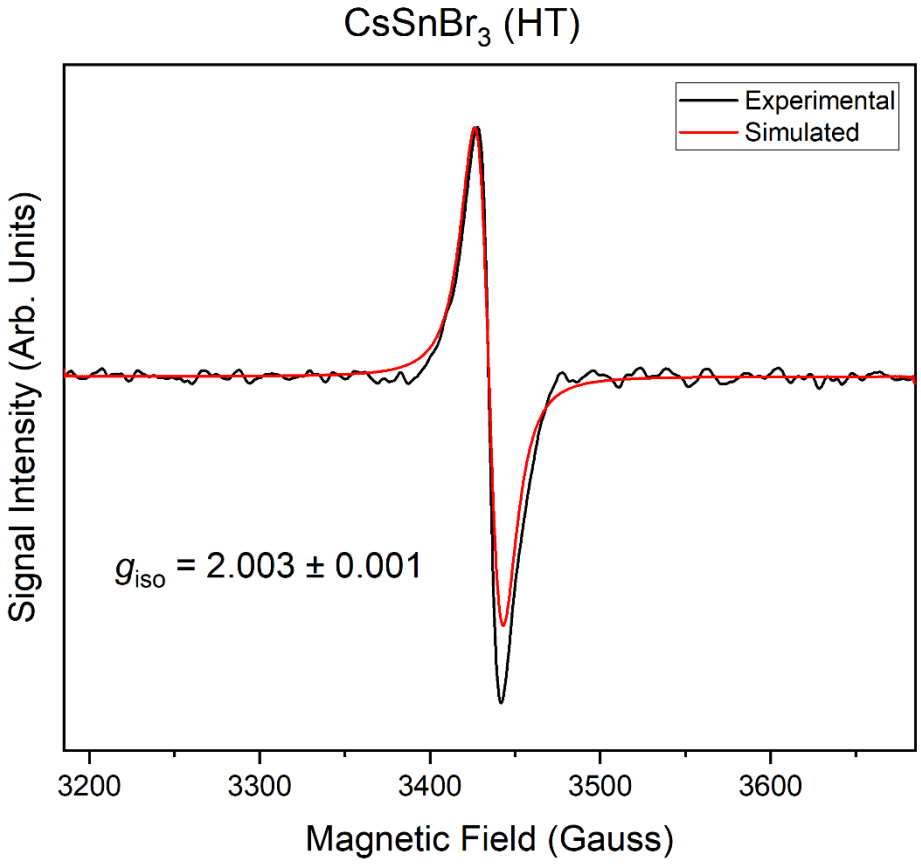

Figure S27. Experimental (black) and fit (red) EPR spectra for HT $CsSnBr_3$.

^{81}Br NQR spectra

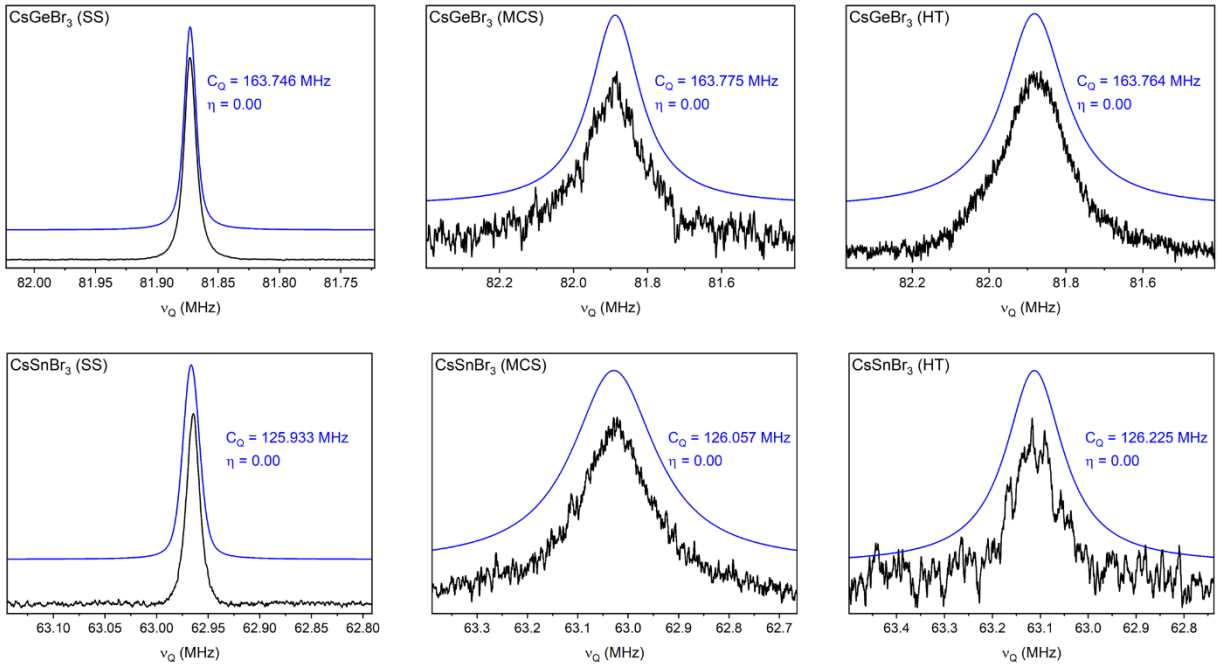

Figure S28. ^{81}Br NQR experimental (black) and simulated fits (blue) for $CsGeBr_3$ and $CsSnBr_3$. Errors for associated measurements are reported in Table 3.

Calculated NMR parameters

$CsSn_xGe_{1-x}Br_3$ MCS

Tables S7-S8. Total calculation time and summary of NMR parameters obtained from CASTEP DFT calculations.

$CsGeBr_3$: 808.03 s

Nucleus		**Shielding Tensor**			**EFG Tensor**	
Species	**No.**	**σ_{calc} (ppm)**	**Ω (ppm)**	**κ**	**C_Q (MHz)**	**η**
Ge	1	1389.70	31.78	0.00	2.310E+00	0.00
Br	1	2173.31	511.65	0.00	1.814E+02	0.01
Br	2	2173.31	511.65	0.00	1.814E+02	0.01
Br	3	2173.31	511.65	0.00	1.814E+02	0.01
Cs	1	5812.39	−11.69	0.00	−5.482E−02	0.00

$CsSnBr_3$: 375.00 s

Nucleus		**Shielding Tensor**			**EFG Tensor**	
Species	**No.**	**σ_{calc} (ppm)**	**Ω (ppm)**	**κ**	**C_Q (MHz)**	**η**
Br	1	2340.42	432.22	0.00	1.477E+02	0.00
Br	2	2340.42	432.22	0.00	1.477E+02	0.00
Br	3	2340.42	432.22	0.00	1.477E+02	0.00
Sn	1	3008.15	0.00	N/A	7.531E−12	N/A
Cs	1	5866.21	0.00	N/A	−6.591E−16	N/A

$CsSn_xGe_{1-x}Br_3$ SS

Tables S9-S10. Total calculation time and summary of NMR parameters obtained from CASTEP DFT calculations.

$CsGeBr_3$: 2143.00 s

Nucleus		**Shielding Tensor**			**EFG Tensor**	
Species	**No.**	**σ_{calc} (ppm)**	**Ω (ppm)**	**κ**	**C_Q (MHz)**	**η**
Ge	1	1402.24	29.61	0.00	2.230E+00	0.00
Br	1	2170.46	518.87	0.00	1.826E+02	0.00
Br	2	2170.46	518.87	0.00	1.826E+02	0.00
Br	3	2170.46	518.87	0.00	1.826E+02	0.00
Cs	1	5813.07	−10.20	0.00	−5.755E−02	0.00

$CsSnBr_3$: 474.24 s

Nucleus		**Shielding Tensor**			**EFG Tensor**	
Species	**No.**	**σ_{calc} (ppm)**	**Ω (ppm)**	**κ**	**C_Q (MHz)**	**η**
Br	1	2339.45	433.10	0.00	1.477E+02	0.00
Br	2	2339.45	433.10	0.00	1.477E+02	0.00
Br	3	2339.45	433.10	0.00	1.477E+02	0.00
Sn	1	3005.62	0.00	N/A	1.472E−12	N/A
Cs	1	5866.09	0.00	N/A	1.580E−15	N/A

$CsSn_xGe_{1-x}Br_3$ HT

Tables S11-S12. Total calculation time and summary of NMR parameters obtained from CASTEP DFT calculations.

$CsGeBr_3$: 1080.02 s

Nucleus		**Shielding Tensor**			**EFG Tensor**	
Species	**No.**	**σ_{calc} (ppm)**	**Ω (ppm)**	**κ**	**C_Q (MHz)**	**η**
Ge	1	1398.57	34.46	0.00	2.267E+00	0.00
Br	1	2175.08	512.56	0.01	1.817E+02	0.01
Br	2	2175.08	512.56	0.01	1.817E+02	0.01
Br	3	2175.08	512.56	0.01	1.817E+02	0.01
Cs	1	5811.93	−7.24	0.00	−5.525E−02	0.00

$CsSnBr_3$: 333.09 s

Nucleus		**Shielding Tensor**			**EFG Tensor**	
Species	**No.**	**σ_{calc} (ppm)**	**Ω (ppm)**	**κ**	**C_Q (MHz)**	**η**
Br	1	2340.04	431.30	0.00	1.477E+02	0.00
Br	2	2340.04	431.30	0.00	1.477E+02	0.00
Br	3	2340.04	431.30	0.00	1.477E+02	0.00
Sn	1	3004.55	0.00	N/A	−2.076E−12	N/A
Cs	1	5865.96	0.00	N/A	−1.603E−15	N/A

References

(1) Hooper, R. W.; Ni, C.; Tkachuk, D. G.; He, Y.; Terskikh, V. V.; Veinot, J. G. C.; Michaelis, V. K. Exploring Structural Nuances in Germanium Halide Perovskites Using Solid-State ^{73}Ge and ^{133}Cs NMR Spectroscopy. *The Journal of Physical Chemistry Letters* **2022**, *13* (7), 1687-1696. DOI: 10.1021/acs.jpclett.1c04033.

(2) *TOPAS-Academic, version 6*; Coelho Software: Brisbane, Australia, 2016.

(3) Fabini, D. H.; Laurita, G.; Bechtel, J. S.; Stoumpos, C. C.; Evans, H. A.; Kontos, A. G.; Raptis, Y. S.; Falaras, P.; Van der Ven, A.; Kanatzidis, M. G.; et al. Dynamic Stereochemical Activity of the Sn^{2+} Lone Pair in Perovskite $CsSnBr_3$. *Journal of the American Chemical Society* **2016**, *138* (36), 11820-11832. DOI: 10.1021/jacs.6b06287.

(4) Tang, L. C.; Huang, J. Y.; Chang, C. S.; Lee, M. H.; Liu, L. Q. New infrared nonlinear optical crystal $CsGeBr_3$: synthesis, structure and powder second-harmonic generation properties. *Journal of Physics: Condensed Matter* **2005**, *17* (46), 7275-7286. DOI: 10.1088/0953-8984/17/46/011.

(5) Sheldrick, G. M. A short history of SHELX. *Acta Crystallographica Section A: Foundations of Crystallography* **2008**, *64* (1), 112-122.

(6) Farrugia, L. J. WinGX and ORTEP for Windows: an update. *Journal of Applied Crystallography* **2012**, *45* (4), 849-854. DOI: https://doi.org/10.1107/S0021889812029111.

(7) Wong, A.; Sham, S.; Wang, S.; Wu, G. A solid-state ^{133}Cs nuclear magnetic resonance and X-ray crystallographic study of cesium complexes with macrocyclic ligands. *Canadian Journal of Chemistry* **2000**, *78* (7), 975-985. DOI: 10.1139/v00-097.

(8) Ha, M.; Karmakar, A.; Bernard, G. M.; Basilio, E.; Krishnamurthy, A.; Askar, A. M.; Shankar, K.; Kroeker, S.; Michaelis, V. K. Phase Evolution in Methylammonium Tin Halide Perovskites with Variable Temperature Solid-State ^{119}Sn NMR Spectroscopy. *The Journal of Physical Chemistry C* **2020**, *124* (28), 15015-15027. DOI: 10.1021/acs.jpcc.0c03589.

(9) Javadi, M.; Michaelis, V. K.; Veinot, J. G. C. Thermally Induced Evolution of "$Ge(OH)_2$": Controlling the Formation of Oxide-Embedded Ge Nanocrystals. *The Journal of Physical Chemistry C* **2018**, *122* (30), 17518-17525. DOI: 10.1021/acs.jpcc.8b04640.

(10) Michaelis, V. K.; Kroeker, S. ^{73}Ge Solid-State NMR of Germanium Oxide Materials: Experimental and Theoretical Studies. *The Journal of Physical Chemistry C* **2010**, *114* (49), 21736-21744. DOI: 10.1021/jp1071082.

(11) Perras, F. A.; Widdifield, C. M.; Bryce, D. L. QUEST—QUadrupolar Exact SofTware: A fast graphical program for the exact simulation of NMR and NQR spectra for quadrupolar nuclei. *Solid State Nuclear Magnetic Resonance* **2012**, *45-46*, 36-44. DOI: https://doi.org/10.1016/j.ssnmr.2012.05.002.

(12) Massiot, D.; Farnan, I.; Gautier, N.; Trumeau, D.; Trokiner, A.; Coutures, J. P. ^{71}Ga and ^{69}Ga nuclear magnetic resonance study of β-Ga_2O_3: resolution of four- and six-fold coordinated Ga sites in static conditions. *Solid State Nuclear Magnetic Resonance* **1995**, *4* (4), 241-248. DOI: https://doi.org/10.1016/0926-2040(95)00002-8.

(13) Clark, S. J.; Segall, M. D.; Pickard, C. J.; Hasnip, P. J.; Probert, M. I. J.; Refson, K.; Payne, M. C. First principles methods using CASTEP. *Zeitschrift für Kristallographie - Crystalline Materials* **2005**, *220* (5-6), 567-570. DOI: doi:10.1524/zkri.220.5.567.65075.

(14) Pickard, C. J.; Mauri, F. All-electron magnetic response with pseudopotentials: NMR chemical shifts. *Physical Review B* **2001**, *63* (24), 245101-245101. DOI: 10.1103/PhysRevB.63.245101.

(15) Yates, J. R.; Pickard, C. J.; Mauri, F. Calculation of NMR chemical shifts for extended systems using ultrasoft pseudopotentials. *Physical Review B* **2007**, *76* (2), 24401-24401. DOI: 10.1103/PhysRevB.76.024401.

(16) Profeta, M.; Mauri, F.; Pickard, C. J. Accurate first principles prediction of ^{17}O NMR parameters in SiO_2: assignment of the zeolite ferrierite spectrum. *J Am Chem Soc* **2003**, *125* (2), 541-548. DOI: 10.1021/ja027124r.

(17) Charpentier, T. The PAW/GIPAW approach for computing NMR parameters: A new dimension added to NMR study of solids. *Solid State Nuclear Magnetic Resonance* **2011**, *40* (1), 1-20. DOI: https://doi.org/10.1016/j.ssnmr.2011.04.006.

(18) Perdew, J. P.; Burke, K.; Ernzerhof, M. Generalized Gradient Approximation Made Simple. *Phys Rev Lett* **1996**, *77* (18), 3865-3868. DOI: 10.1103/PhysRevLett.77.3865.
(19) Makuła, P.; Pacia, M.; Macyk, W. How To Correctly Determine the Band Gap Energy of Modified Semiconductor Photocatalysts Based on UV–Vis Spectra. *The Journal of Physical Chemistry Letters* **2018**, *9* (23), 6814-6817. DOI: 10.1021/acs.jpclett.8b02892.
(20) Stoll, S.; Schweiger, A. EasySpin, a comprehensive software package for spectral simulation and analysis in EPR. *Journal of Magnetic Resonance* **2006**, *178* (1), 42-55. DOI: https://doi.org/10.1016/j.jmr.2005.08.013.